



Machine learning-based modeling of the coupling effect of strain rate and temperature on strain hardening for 5182-O aluminum alloy

Hongchun Shang^a, Pengfei Wu^a, Yanshan Lou^{a,*}, Jizhen Wang^b, Qiang Chen^c

^a School of Mechanical Engineering, Xi'an Jiaotong University, 28 Xianning West Road, Xi'an, Shaanxi, 710049, China

^b Aviation Key Laboratory of Science and Technology on Structure Impact Dynamics, Aircraft Strength Research Institute of China, Xi'an, Shaanxi, 710065, China

^c Southwest Technology and Engineering Research Institute, 33 Yuzhou Road, Chongqing, 400039, China



ARTICLE INFO

Associate Editor: Yongjie Jessica Zhang

Keywords:

Strain rate hardening
Thermal softening
Artificial neural network

ABSTRACT

This research characterizes the dynamic hardening behavior of an aluminum alloy sheet of 5182-O for the coupling effect of strain rate and temperature. Tests are carried out for dogbone specimens at different loading conditions to experimentally characterize the strain rate hardening and thermal softening effect for the alloy. The behaviours are then modeled by the Johnson-Cook, Zerilli-Armstrong and Lim-Huh models. In addition, the FEA-friendly polynomial model and artificial neural network (ANN) model are used to describe the highly non-linearity and coupling of strain hardening. Factors affecting ANN predicting accuracy and numerical computing efficiency are comprehensively studied including network structure, parameter settings and optimization algorithms. All the analytical and ANN models are also implemented into ABAQUS/Explicit to numerically compute the reaction force of tensile tests of dogbone specimens. The strain hardening curves are predicted by the analytical and ANN models for the comparison with experimental measurements to evaluate their performance. The experimental results show that the strain rate is slightly negative at room temperature, while the strain rate effect turns to be positive as temperature rises. The comparison of the flow curves between prediction and experiments reveals that the coupling effect is reasonably illustrated by the proposed polynomial model and the ANN model illustrates the flow curves with the dramatically much better accuracy than all the other models. The numerically predicted reaction forces prove that the ANN model accurately illustrates the load capability with the best agreement among the models studied in this research. The numerical computation also shows that the numerical computation efficiency of the ANN model is slightly reduced compared with analytical models, but the reduction is not much and worthwhile compared with the high accuracy of ANN.

1. Introduction

The application of lightweight materials in auto parts is considered as an important solution to the efficient use of energy and the reduction of carbon dioxide emissions. However, the application of aluminum sheet in parts such as automobile bodies and engines is greatly restricted due to low room temperature formability. To overcome this restriction, the superplastic and isothermal forming process of aluminum alloy sheets have attracted widespread attentions. One of the concerns in warm forming of aluminum alloy is how to accurately characterize the highly non-linearity dynamic hardening behavior and establish a suitable constitutive model.

The yield stress, strength and hardening behavior of materials are affected by many factors, such as temperature, strain rate and stress

state. Their effect needs to be accurately modeled to ensure reliable analytical and numerical analysis and design of warm forming for aluminum alloys. In last decades, researchers proposed or improved many constitutive models to describe plastic flow behavior that depends on different state variables. According to the characteristics of modeling, these constitutive models are divided into phenomenological and physical-based ones. The latest progress of physical-based constitutive models is inspired by in-depth understanding of underlying physics at the atomic level (Iftikhar et al., 2021), dislocation dynamics (Buzolin et al., 2021), grain evolution (Zhu et al., 2021), etc. In terms of phenomenological constitutive models, the Johnson-Cook (JC) model is the most widely used because of its simple structure and fewer parameters to be calibrated (Johnson and Cook, 1983). Zerilli and Armstrong (1987) proposed two different expressions for the hardening

* Corresponding author.

E-mail address: ys.lou@xjtu.edu.cn (Y. Lou).

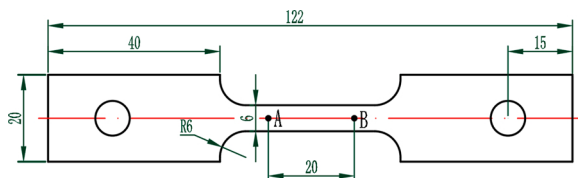


Fig. 1. Dogbone specimen geometries.

characteristics of BCC and FCC crystal structure materials, which are denoted as ZA BCC and ZA FCC. The Lim-Huh (LH) model can accurately express the change of strain hardening with strain rate, because the strain rate hardening effect changes with plastic strain (Huh et al., 2014).

At present, the artificial neural network (ANN) has been further developed through the combination with other disciplines. ANN is a data-driven nonlinear mapping model, which has a wide range of applications in predictive evaluation, pattern recognition, signal processing and other fields. In the field of metal forming, Kessler et al. (2007) introduced the ANN model into the finite element analysis to predict rheological behavior. Since then, ANN has achieved vigorous development in the field of metal plasticity, including process parameter optimization, polycrystalline micromechanics and macroscopic constitutive models. For example, in terms of process parameter optimization, Kohar et al. (2017) developed a new frame to design an optimized front rail which greatly increases the absorbed collision energy. Response surface method with ANN model and simulated annealing optimization technology was used to optimize the structure for lightweight design. Based on the results of sheet metal bending tests, Fu et al. (2010) proposed a three-layer back propagation neural network (BPNN) to solve a discrete engineering problem involving multiple parameters. In the field of polycrystalline micromechanics, Ali et al. (2019) successfully combined the ANN model and the rate-dependent CPFEM to predict the stress-strain behavior and texture evolution of AA6063-T6. To improve the accuracy of sheet metal forming simulation, Yamanaka et al. (2020) corrected the constitutive model using the results of multiaxial tensile tests. In their research, they proposed two different deep neural networks to estimate biaxial stress-strain curves with high accuracy. Mayer et al. (2021) used molecular dynamics simulations to characterize material properties at elastic stage, and then approximated it through the ANN model. Settgast et al. (2020) proposed a new hybrid multi-scale neural network approach to describe irreversible material behavior at the macroscopic scale. Muhammad et al. (2021) used the microstructure characteristics as input to train the ANN model, and successfully predicted the evolution of local strains, plastic anisotropy and failure during tensile deformation.

Another very important application of neural network is to establish a multi-factor coupled macroscopic constitutive model. Among them, the characterization of non-monotonic dynamic hardening behavior is one of the typical cases. The conventional hardening models cannot model complex plastic behavior because it is difficult to illustrate nonlinearly coupled effects among factors. ANN is considered to be an effective means to overcome these difficulties. Jenab et al. (2016) obtained hardening curves with different tensile directions from rolling direction and different strain rates ($0.001/s \sim 1000/s$) through experiments of AA5182-O material. The genetic algorithm was used to calibrate the parameters in traditional constitutive models. Then ANN was trained to predict the dynamic hardening characteristics of the alloy. Mozaffar et al. (2019) showed that deep learning methods can predict efficiently and precisely material plasticity, which is fundamentally different from the century-old theory of continuum plasticity. Li et al. (2019) introduced a neural network based on the JC model to reflect the non-monotonic effects of temperature and strain rate on the strain hardening of DP steel. Jordan et al. (2020) proposed a machine learning model with Bayesian regularization back propagation algorithm to

describe the temperature and strain rate dependent response of polypropylene. Regarding other aspects of the plastic constitutive model, Palau et al. (2012) used the traditional J_2 plastic model to generate training data for monotonic, cyclic and random loading paths to train shallow networks. Zhang and Mohr (2020) mathematically re-derived the algorithm description of the Mises plasticity with isotropic hardening, so that the relationship between strain and stress could be modeled by neural network functions. For the nonlinear strain path, Jang et al. (2020) used round cup stretching simulation to predict the cup shape. It was found that the simulation results based on the ANN model were in good agreement with the simulation results of the conventional constitutive model based on J_2 . For the modeling of plane stress plasticity for arbitrary loading paths, Gorji et al. (2020) showed that the gated recurrent units based networks can capture the nonlinear characteristics of the anisotropic Yld2000 plasticity model with homogeneous anisotropic hardening. Pandya et al. (2020) described the plastic response of 7075 aluminum alloy at different rates during the hot stamping process by a neural network to couple the effects of strain rate and temperature into the Hosford-Coulomb fracture model. The forming limit curve was used to describe the maximum in-plane strain applied to the sheet metal before necking occurs. Bonatti and Mohr (2020) proved that the neural network model provided a computationally efficient method to describe the impact of non-proportional loading. A Marciniak-Kuczynski model based on finite elements was established, and the forming limit of DP780 steel was characterized by virtual experiments.

The response of materials to temperature changes is controlled by complex mechanisms, such as thermal softening, dynamic recovery, dynamic recrystallization and dynamic strain aging (DSA). In addition to the common thermal softening phenomenon, the thermal effect of DSA also exists in many metal materials. The DSA effect of Al-Mg alloy (AA5xxx) alloy is due to the complex stress-strain behavior caused by flow dislocation and atomic interaction (Kabirian et al., 2014). DSA shows obvious jaggedness on the stress-strain curve. Negative strain rate sensitivity is another sign that DSA is activated within a certain temperature and strain rate range. In the process of simulating the stress-strain response, the complex strain rate sensitivity behavior of Al-Mg alloys under different temperatures and strain rate ranges is considered to be the biggest challenge for analytical modeling. Research by Khan and Baig (2011) showed that the strength of AA5182-O decreased when the strain rate increases from the quasi-static range to the dynamic range. Abedrabbo et al. (2007) reported that the strain rate sensitivity of AA5182-O and AA5754-O increased significantly with rising temperature although they were not sensitive at room temperature.

In summary, the ANN model is shown to be very high accuracy for the modeling of the strain rate and thermal effect on flow curves of metals. However, computation cost has not been comprehensively investigated for the ANN model. Besides, the ANN model is not compared with popular analytical models in terms of accuracy and computation efficiency. Both the analytical and ANN models are not evaluated for a material with dramatically strong coupling effect between strain rates and temperature on flow curves.

Therefore, the effects of strain rate on the dynamic hardening behavior of 5182-O alloy at distinct temperature obtained through experimental studies are analytically modeled by the JC, ZA and LH models in this paper. The coupling of strain rate and thermal effect is also simulated by a newly proposed FEA-friendly polynomial model and ANN. Factors affecting the accuracy of ANN are comprehensively studied. All models are implemented in numerical simulations to predict the reaction force at different stretching velocities and temperatures. Their prediction accuracy is evaluated by comparing the predicted flow curves with experimental results at different loading conditions. The computation efficiency and the other key factors of numerical simulation are also compared for all the models to comprehensively evaluate the models.

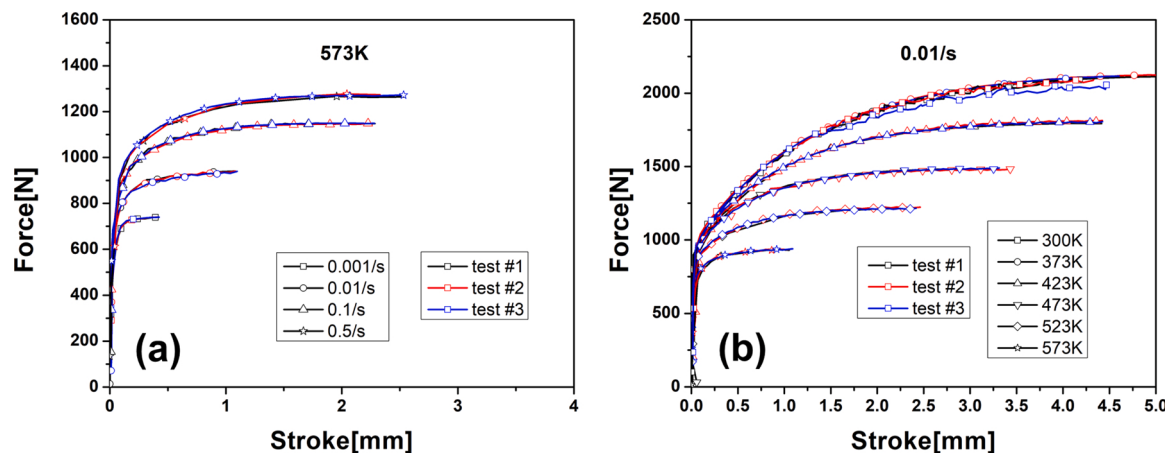


Fig. 2. Repeatability check of experiments: (a) force-displacement curves at 573 K of different strain rates, (b) force-displacement curves at a strain rate of 0.01/s for different temperatures.

2. Experiments

The 5182-O aluminum alloy is selected as the research target for the characteristics of strain rate and temperature on hardening. Experimental samples designed in Fig. 1 are cut from 1.25 mm thick sheets along the rolling direction. The dogbone specimen has a parallel tensile gauge of 30 mm while the stroke is measured with an initial gauge length of 20 mm as indicated by AB in Fig. 1. The width and thickness of the gauge section of the processed dogbone specimens are measured before the experiment, which shows that the dimension accuracy is high enough and acceptable for the tests.

The dynamic hardening characteristics of the 5182-O sheet are obtained by uniaxial tensile test on a universal testing machine. The experiment covers a wide temperature range from 300 K to 573 K with another four testing temperatures of 373 K, 423 K, 473 K, 523 K inbetween. The stretching strain rate ranges between 0.001/s and 0.5/s. To achieve the loading rate of 0.001/s, 0.01/s, 0.1/s and 0.5/s, the crosshead speed is controlled to be 1.8, 18, 180 and 900 mm/min. At least four repeating tests are conducted for each condition to ensure the reliability of the tests. Accordingly, there are totally 96 experiments to investigate the strain rate and temperature effect. The specimens are heated in an INSTRON environmental chamber where the temperature is controlled by a type N thermocouple. The temperature controller installed on the chamber ensures that the error is ± 0.5 °C. After the temperature is raised to the specified temperature, the sample is held for 90 s before the specimen is loaded. During the tests, digital image correlation (DIC) technology is used to accurately measure the deformation with respect to loading force. The specimens are sprayed with white paint as a base, and then randomly sprayed with black spots. The deformation process of the specimens is recorded by the XTOP DIC system with the help of the applied spots. The acquisition frequency of the two-camera DIC system with a resolution of 2448×2050 is adjusted so that 100–200 images are recorded per set of experiments. A virtual extensometer with an initial gauge length of 20 mm is generated in DIC analysis to measure the strokes with respect to loading force. The signal from the load cell is synthesised in the DIC system so that load and deformation are recorded simultaneously with the identical rate. The load-stroke curves before the maximum load are compared in Fig. 2 (a) at 573 K with different strain rates and Fig. 2 (b) at 0.1/s with different temperatures. The comparison indicates very good repeatability and high reliability of the tests.

3. Experimental results

The experimental force-displacement curves before the maximum force are compared in Fig. 3 at six different temperatures and four

different loading speeds. Then the true stress-true plastic strain curves of 5182-O are calculated from the force-displacement curve as compared in Fig. 4.

It is observed that at room temperature 300 K, the stress intensity of the material decreases with the increase of the stretching speed due to the influence of the DSA effect. This is demonstrated by the discontinuous strain distribution and shear band measured by DIC in Fig. 5 at 300 K. For higher temperatures, the plastic deformation is much more homogeneous and shear bands disappear, which indicates positive strain rate effect at high temperatures. The performance of DSA is usually related to the microstructure, which affects the dynamics of the nucleation and propagation of deformation bands (Anna et al., 2016). A lot of research was conducted to reveal the mechanisms of DSA, the dynamic interaction between mobile dislocations and solid solution atoms under certain load conditions, such as Mg in Al-Mg based alloys. When the temperature is 373 K, the stress increases as the strain rate rises from 0.001/s to 0.01/s and then decreases with the strain rate from 0.01/s to 0.5/s. When the temperature further rises to 423 K, the strength increases with strain rate from 0.001/s to 0.1/s and then decreases with strain rate when the strain rate is higher than 0.1/s. The strain rate sensitivity at 373 K and 423 K is somewhat complicated. For the temperature higher or equal to 473 K, the strain rate strengthening effect is more significant. That is, experiments show the positive strain rate sensitivity of this alloy at 473 K or higher and the positive strain rate sensitivity is more apparent for higher testing temperature. It is concluded that the strain rate effect is different at different temperatures. This complex strain rate sensitivity with temperature effect cannot be reasonably described by conventional models, such as the JC function which treats the strain rate sensitivity and thermal softening separately. Models should be selected or proposed to describe the coupled effect.

Besides, it is observed in Fig. 4 that there is little effect of strain rate on the yield stress at zero plastic strain when the temperature is low at 300 K, 373 K and 423 K. The ZA model reviewed in the section below describes that the yield stress at zero plastic strain is insensitive to strain rates for FCC materials. The experimental results at 300 K, 373 K and 423 K prove the reasonability of the ZA model for the modeling of strain rate sensitivity for FCC metals. However, when the temperature is higher than 423 K, especially for tests at 523 K and 573 K, higher strain rate does not only correspond to higher strength, but also raises the yield stress at zero plastic strain. It means that the ZA model is not applicable for the modeling of strain rate effect at higher temperature for 5182-O.

Finally, the experimental results are compared in Fig. 6 at different temperatures under the same strain rate. From these results, it is easy to recognise the non-uniform decrease in the flow stress of the material with increasing temperatures, which is associated with the significant temperature softening effect. In general, the strain before the maximum

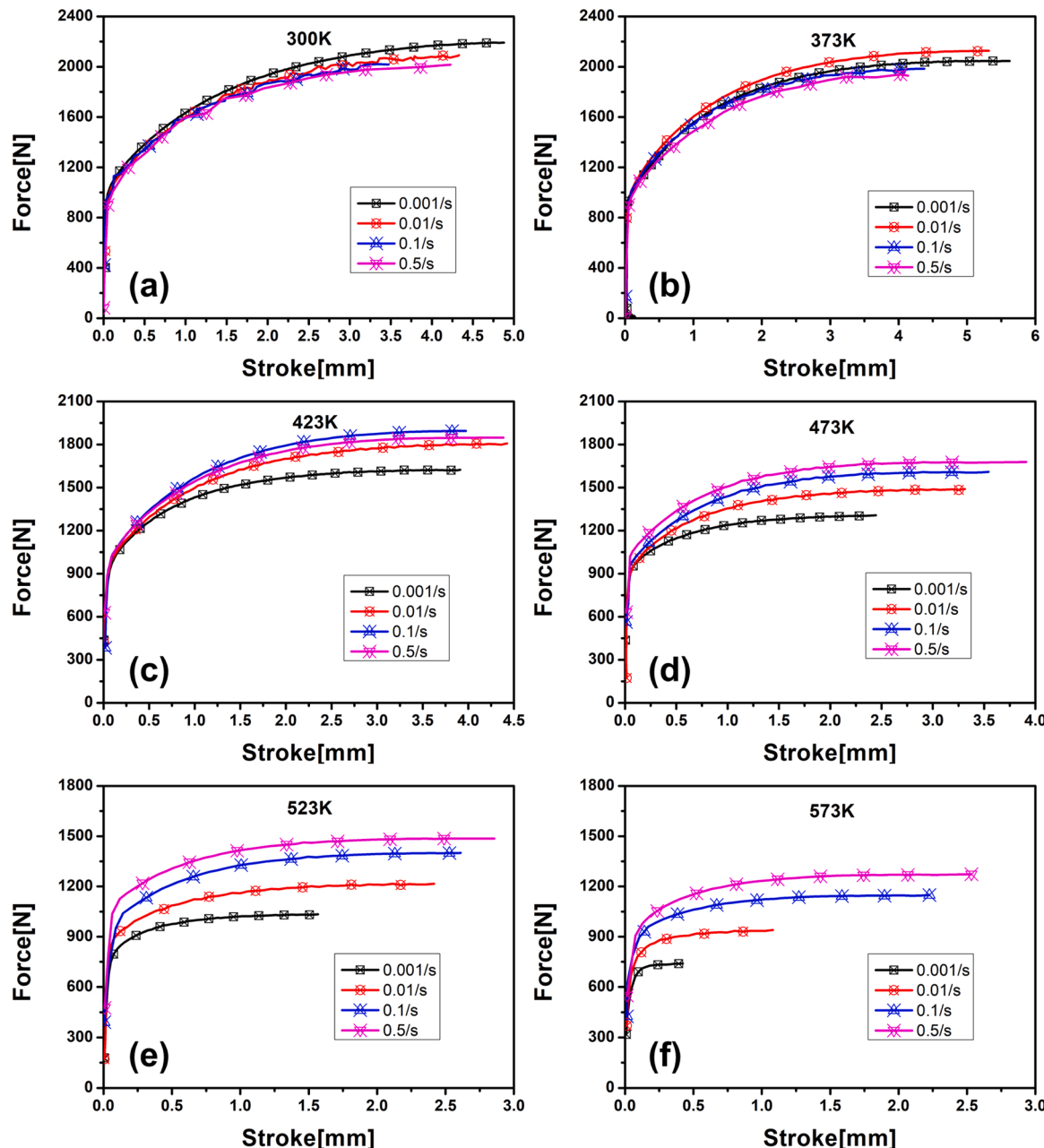


Fig. 3. Force-displacement curves for different temperatures and loading speeds of (a) 300 K, (b) 373 K, (c) 423 K, (d) 473 K, (e) 523 K and (f) 573 K.

force, or necking strain, also decreases with increasing temperature. When the temperature reaches 573 K, the necking strain with a strain rate of 0.001/s is only 0.018. The comparison between the four graphs shows that the higher strain rate enhances the strain at uniform elongation above 473 K. This observation indicates that a high stamping speed may improve the formability of the alloy at high temperature. Besides, Fig. 6 shows that the elevated temperature degrades the strength of the materials more effectively at large strain than small one.

To sum up of 24 sets of experiments, the strain rate sensitivity and thermal softening is very complicated and their effect is coupled with each other. The coupling effect cannot be easily modeled by conventional models, such as JC and ZA. Advanced approaches should be introduced to improve the modeling accuracy of the coupled strain rate and thermal softening effect.

4. Hardening model for coupled strain rate and thermal effect

The flow behavior of materials in the metal forming process is greatly affected by strain, strain rate and temperature. The constitutive models proposed or improved to describe the influence of strain rate and temperature on the flow curves are divided into two categories: phenomenological constitutive models and physics-based constitutive models. Since the phenomenological constitutive models empirically describe the hardening behavior, these constitutive models have fewer parameters. Therefore, they are easier to apply in numerical simulation, such as JC model, LH model, etc. The physics-based constitutive models can reflect the macroscopic state and the microscopic evolution. Almost all physics-based constitutive models have introduced thermodynamic theory and dislocation kinetic theory, such as ZA model. Three constitutive models are presented in Appendix B, and they are suitable for the tensile data in the literature (Huh et al., 2014).

According to experimental results, 5182-O alloy is negative sensitive

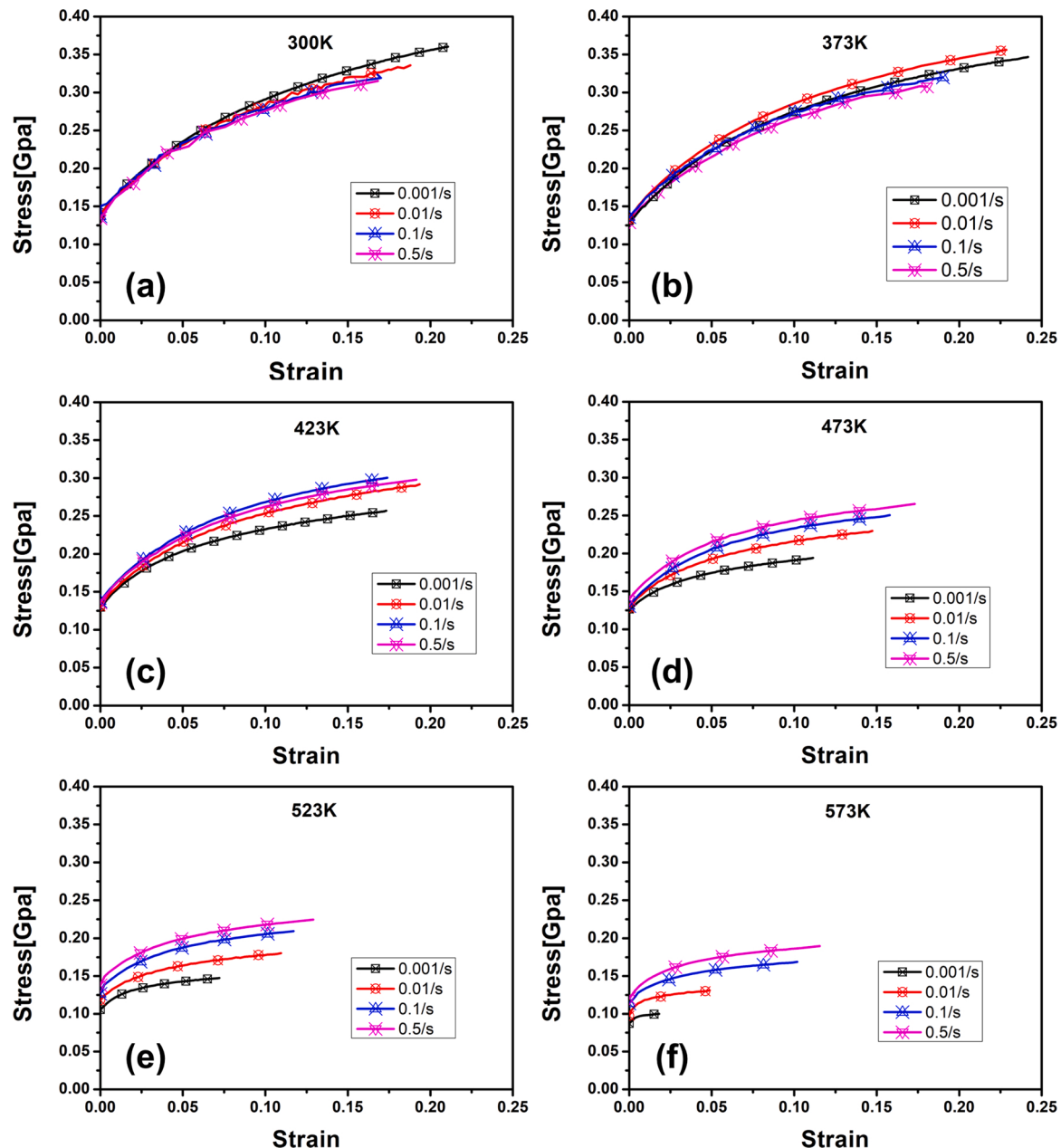


Fig. 4. Experimental stress-strain curves at different strain rates under the same temperature of (a) 300 K, (b) 373 K, (c) 423 K, (d) 473 K, (e) 523 K and (f) 573 K.

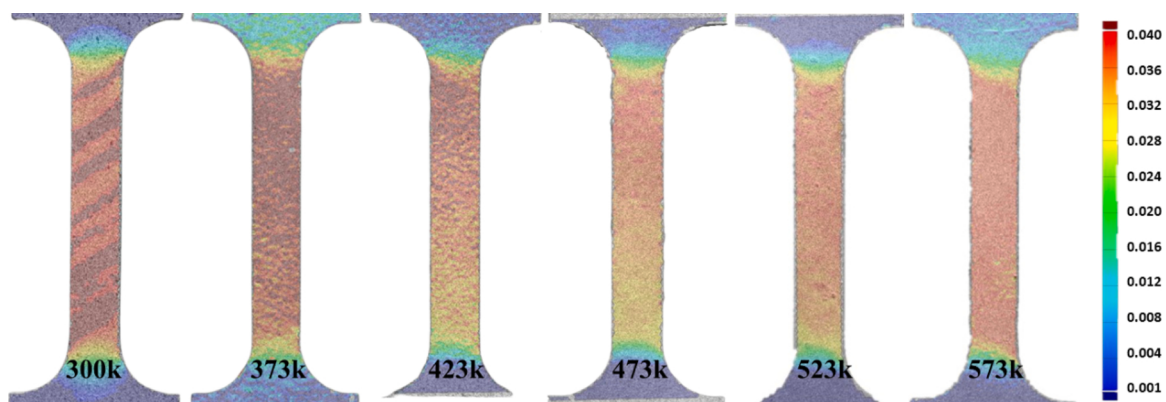


Fig. 5. The effective surface strain field before necking (0.01/s).

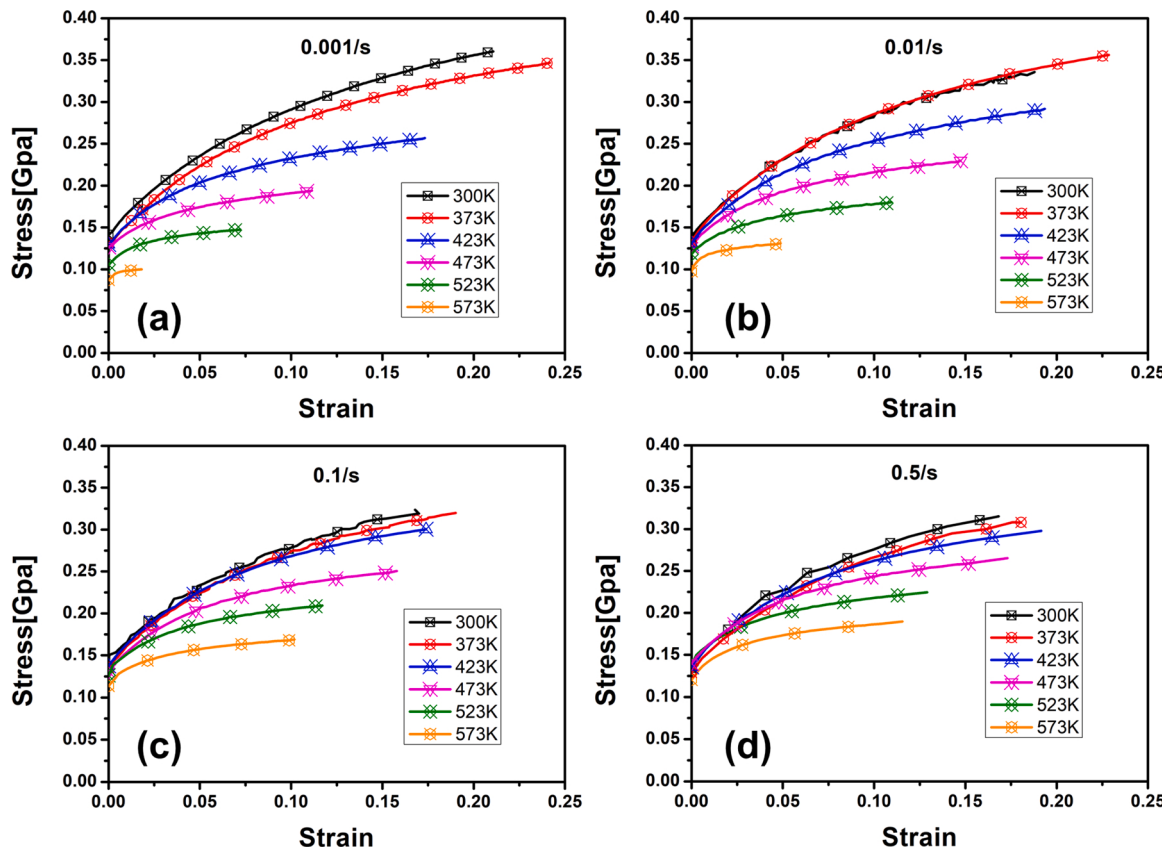


Fig. 6. Experimental stress-strain curves at different temperatures under the same strain rate of (a) 0.001/s, (b) 0.01/s, (c) 0.1/s and (d) 0.5/s.

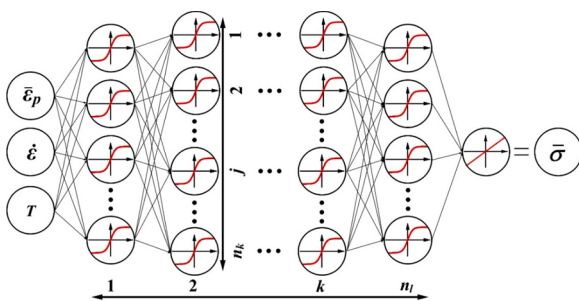


Fig. 7. Artificial neural network structure.

to strain rate at room temperature, and strong positive strain rate sensitivity is observed at high temperature. The strain rate sensitivity is affected by deformation temperature. Most dynamic strain hardening models does not consider the coupled effect, such as the JC model. The ZA model considers the coupled effect together, but the yield stress value calibrated by the ZA FCC model does not change. The LH model is capable of the coupling effect of strain rate and temperature. However, it is very difficult to compute its partial derivative as computed in Appendix A, which makes its numerical application very difficult. Therefore, it is necessary to propose a simple constitutive model to consider the interaction of temperature and strain rate effect. The strain hardening part is retained according to the JC model while the strain rate and temperature influencing factors are considered in the form of a coupled polynomial (CP). Then the newly proposed model reads as below:

$$\begin{aligned} \sigma(\epsilon, \dot{\epsilon}, T) = & (A + Be^n) \cdot [1 + C(\dot{\epsilon}^*) + DT^* + E(\dot{\epsilon}^*) \cdot T^* + F(\dot{\epsilon}^*)^2 \cdot T^* \\ & + G(\dot{\epsilon}^*) \cdot T^2] \end{aligned} \quad (1)$$

$$\text{where } T^* = 1 - \left(\frac{T - T_r}{T_m - T_r} \right)^m, \dot{\epsilon}^* = \ln \frac{\dot{\epsilon}}{\dot{\epsilon}_0}$$

With the newly proposed dynamic hardening model, it is apparent that the strain rate hardening effect is different at different temperatures. Accordingly, it is expected to provide better modeling of the dynamic hardening behavior of 5182-O. Besides, its computation of derivatives is relatively simple thereby resulting in easy implementation into numerical simulation.

5. Machine learning

There are many existing models to consider the strain rate and thermal effect on strain hardening behavior of materials. However, experimental results in Section 3 show that the strain rate and thermal effect on hardening behavior of AA5182-O is highly nonlinear and their effect is strongly coupled together. The highly nonlinear and coupling effect of strain rate and temperature effect cannot be accurately predicted by the traditional models. On the contrary, ANN is a data-driven nonlinear mapping model that simulates the processing mechanism of complex information. Therefore, this research employs the ANN model for the analytical and numerical modeling of this highly nonlinear problem, and compares the predicting results with the predicting results of popular theory-driven models. Due to its simple structure and stable working status, BP network is widely used in many neural network models. The structure is shown in Fig. 7 for the modeling of coupling effect.

The number of neurons in each hidden layer and the number of hidden layers are defined according to the number of samples and the complexity of the mapping relationship between input and output data. If the calculated output error exceeds the expected value, the back propagation of the error starts. The error is distributed to all the units of each layer through backpropagation as the basis for correcting the

Table 1

Equation of different types of activation functions.

Name of function	Function equation
Sigmoid function (logsig)	$y = 1/(1 + e^{-x})$
Tangent sigmoid function (tansig)	$y = \tanh(x)$
Linear function (purelin)	$y = x$

weight. This process is carried out in a cycle/loop to adjust the weights and referred as the network training. It continues until the error of the network output is reduced to an acceptable level. Appendix C shows two optimization algorithms of BP neural network. When the node number in the input layer is n , the training process can be described as follows:

- Step 1. Data normalization. The MinMaxscaler technology projects all input variables into the interval [-1, +1]:

$$\bar{x}_i = 2 \times \frac{x_i - x_{\min}}{x_{\max} - x_{\min}} - 1, (i = 1, \dots, n) \quad (2)$$

The maximum and minimum values of the input variables are expressed as x_{\max} and x_{\min} . x_i is normalized to \bar{x}_i as the input variable according to Eq. (2).

- Step 2. Computation from the input layer to the first hidden layer. It should be confirmed that the number of neurons in the first hidden layer is more than the number of input variables to prevent the loss of input information. If the neuron number of the first hidden layer is n_1 , the computation is conducted by Eq. (3) below.

$$y_j^{(1)} = f^{(1)} \left(\sum_{i=1}^n w_{ji}^{(1)} x_i + b_j^{(1)} \right), (j = 1, \dots, n_1) \quad (3)$$

where $w_{ji}^{(1)}$ and $b_j^{(1)}$ are respectively the weight matrix and threshold vector for the first hidden layer. Above are the activations of the first layer calculated by input values. f represents the activation function, which roughly includes logistic sigmoid function, tangent sigmoid function, and linear transfer function.

- Step 3. Computation of the subsequent k th hidden layer ($k = 2, \dots, n_l$). If the $(k-1)$ th and k th layers have $n_{(k-1)}$ and n_k neurons respectively, then the k th hidden layer is calculated as:

$$y_j^{(k)} = f^{(k)} \left(\sum_{i=1}^{n_{k-1}} w_{ji}^{(k)} y_i^{(k-1)} + b_j^{(k)} \right), (j = 1, \dots, n_k) \quad (4)$$

- Step 4. Computation of the output layer from the last hidden layer. For this research, there is only one output, the yield stress $\bar{\sigma}$. If there are n_n neurons of the last hidden layer, then the output layer is computed with the equation below:

$$\bar{\sigma} = f^{(o)} \left(\sum_{i=1}^{n_n} w_i^{(o)} y_i^{n_n} + b^{(o)} \right) \quad (5)$$

where $w_i^{(o)}$ represents the connection weights from the hidden layer to the output layer, $b^{(o)}$ stands for the thresholds of the neuron, $\bar{\sigma}$ stands for the output data.

- Step 5. Inverse normalization of the output layer. The output is obtained by inverse linear scaling the interval [-1,1]. The mean square error (MSE) is minimized through a gradient descent training algorithm:

$$MSE = \frac{1}{N} \sum_{i=1}^N (\bar{\sigma}_{exp} - \bar{\sigma}_{pred})^2 \quad (6)$$

where $\bar{\sigma}_{exp}$ is the experimental value measured and $\bar{\sigma}_{pred}$ is the neural network training output or prediction. N is the total number of experimental data at different loading conditions.

6. Parameter study for ANN

The three input variables $[\bar{\epsilon}_p, \dot{\epsilon}, T]$ of the neural network correspond to the intervals [0,0.25], [0.001,0.5], [298,573], respectively. The output layer is one neuron, which is the equivalent stress corresponding to different state variables. In the training process, it is found that there are several factors affecting the predicting accuracy of the BP neural network, but these factors have not been comprehensively investigated:

- (1) Parameters, such as the number of hidden layers and the neuron number of each layers, must be properly selected to improve the fitting accuracy. However, it is still inconclusive about how to select these important parameters;
- (2) The accuracy of data fitting is determined by the overall distribution of weights and thresholds. The traditional method of obtaining weights and thresholds is to randomly set the initial values. Then they are optimized during training through the BP algorithm;
- (3) The BP algorithm is based on the gradient descent method, which leads to local optimal problems. Therefore, appropriate initial weights and thresholds should be selected to prevent non-convergence or falling into local extreme points.
- (4) There are generally three type of activation functions: tangent sigmoid, logistic sigmoid, linear transfer. It is rarely investigated about which function provides better prediction for the coupling effect.

The factors above are first comprehensively investigated according to the ANN predicting accuracy for the experimental data in Fig. 4. 1562 experimental data points are extracted from 72 sets of tests with different temperatures and strain rates. According to Pandya et al. (2020), 90 % of these experimental data points are randomly selected as the training set for the ANN model. The predicting accuracy is represented by the root mean square error (RMSE) computed by

$$RMSE = \sqrt{\frac{1}{N} \sum_{i=1}^N (y_{exp} - y_{pred})^2} \quad (7)$$

where y_{exp} is the observed data, y_{pred} is the predicted data, and N is the number of observations. In order to improve the prediction accuracy, the RMSE should be as small as possible. For the calibration, the results for weights and thresholds are different for different calibration even with the identical structure of the network. Thus, the RMSE is computed as the mean value of 20 calibrated results for the network of the same structure.

There are several parameters during training of a BP network, such as the epochs, the learning rate and the momentum. Under the same network structure, different parameters have a great impact on the calibration results. First, the best fit for the number of epochs needs to be determined. After the pilot-study, the epoch range is between 100 and 10,000. In order to prevent over fitting, the number of the epochs is limited to 3000 in the model. Second, the learning rate and momentum are important parameters in the training processes. If the BP neural network does not have adaptive values for learning rate and momentum, it may perform poorly (Tsai and Lee, 2011). If the selected learning rate value is low, the convergence speed is very slow; if the selected learning rate value is too high, it may cause violent oscillations in the sample

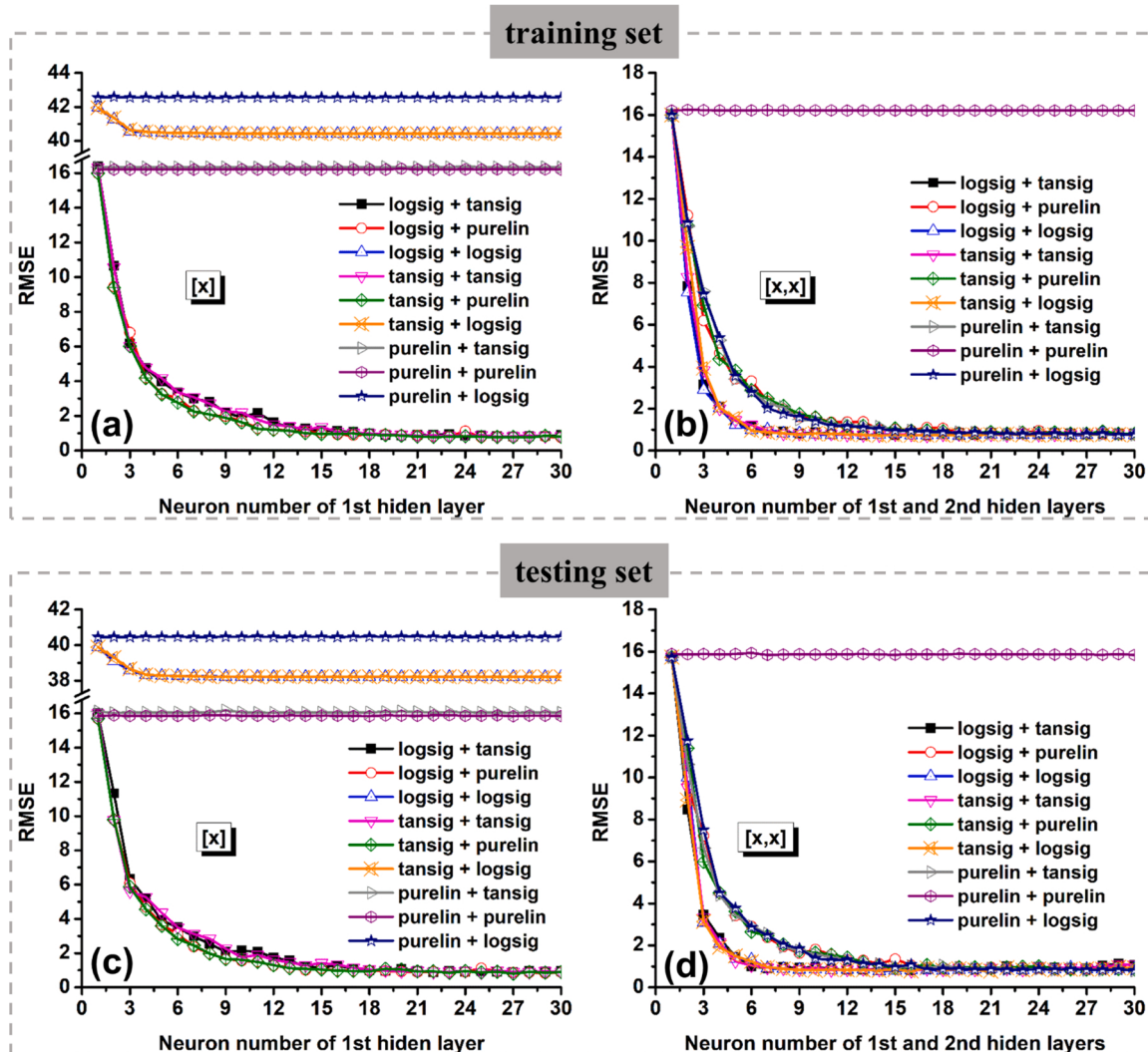


Fig. 8. The RMSE comparison of activation functions: (a) training set-single hidden layer (b) training set-two hidden layers (c) testing set-single hidden layer. (d) testing set-two hidden layers.

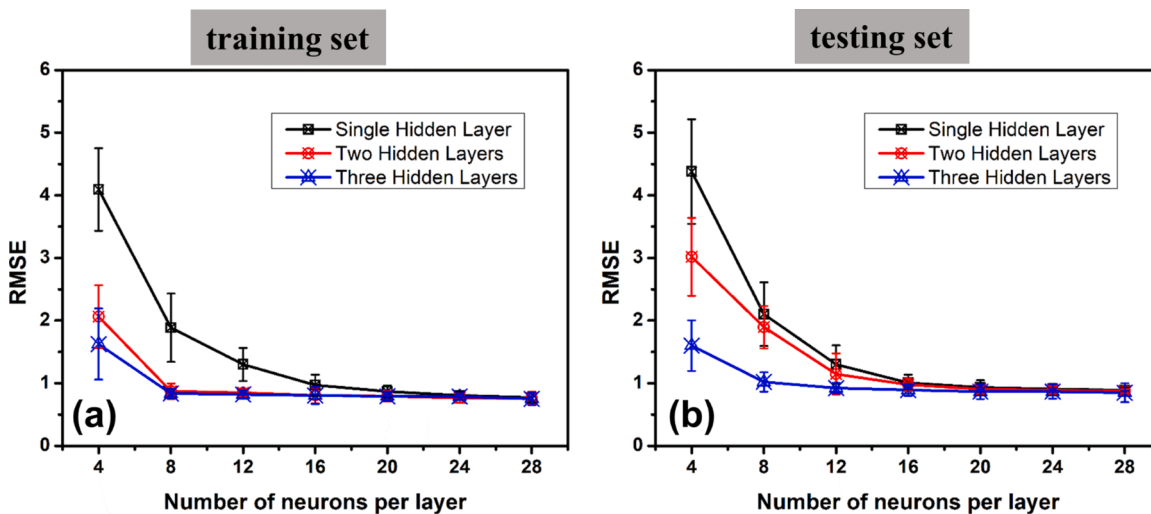


Fig. 9. The RMSE comparison of single-layer, two-layer and three-layer network with the same number of neurons per layer: (a) training set (b) testing set.

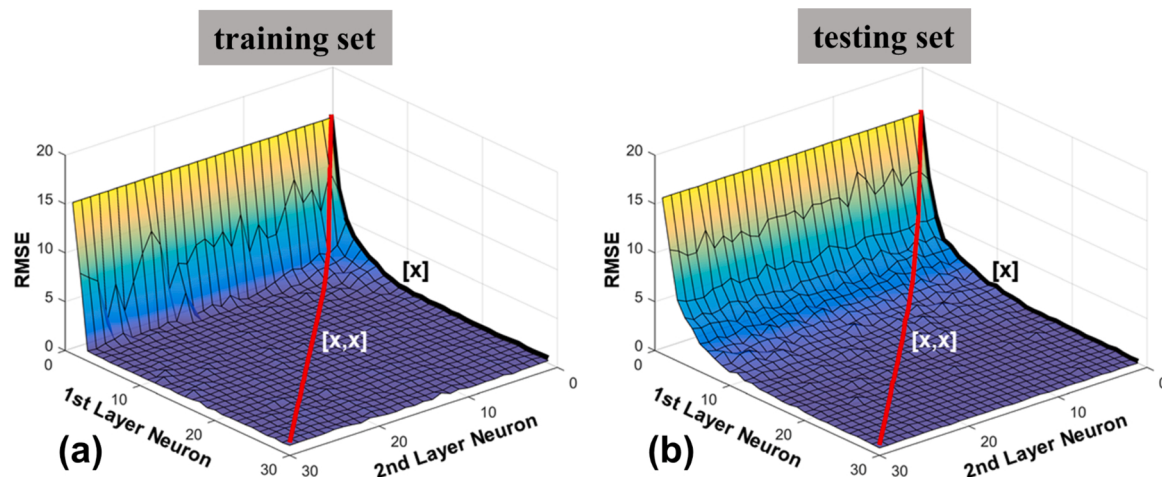


Fig. 10. Effect of neuron numbers on the predicting accuracy for the two-hidden-layer BP network: (a) training set (b) testing set.

Table 2
The selected ANN models structure.

Parameter Number	Number of Hidden Layers	Structure
21	1	3-4-1
	2	3-2-3-1
	3	3-2-1-3-1
41	1	3-8-1
	2	3-4-4-1
	3	3-3-4-2-1
61	1	3-12-1
	2	3-2-13-1
	3	3-4-4-4-1
81	1	3-16-1
	2	3-6-7-1
	3	3-5-6-3-1
101	1	3-20-1
	2	3-7-8-1
	3	3-6-7-3-1
121	1	3-24-1
	2	3-14-4-1
	3	3-5-6-8-1
141	1	3-28-1
	2	3-6-12-1
	3	3-7-6-8-1

training process, and the sample training cannot be completed for the worst case. Momentum makes the bumps in the error surface smoother by referring to the previous weights. Through different adjustments, the best combination of learning rate and momentum is 0.01 and 0.9, respectively.

Before the evaluation of network structures, it needs to compare the predictability of different activation functions. Three types of activation functions are widely used for BP networks as summarized in Table 1, which are logistic sigmoid (logsig), tangent sigmoid (tansig) and linear (purelin) transfer functions. The activation function is generally identical from the input layer to the last hidden layer, and the last hidden layer to the output layer uses a different activation function. Therefore, there are nine different combinations of activation functions. These nine combinations are compared according to their predicting errors of the training/testing sets for the one-hidden-layer and two-hidden-layer BP networks denoted by [x] and [x, x] in Fig. 8, respectively. Here x denotes the neuron number of the corresponding hidden layers. The comparison between Fig. 8 (a) and (c) shows that for the combination of the purelin + logsig, logsig + logsig and tansig + logsig of the single-hidden-layer network, the RMSE of the training set is between 40–43, but the RMSE of the testing set is between 38–41. It is found that except for the obvious deviations of the above three combinations, the conclusions drawn from the other combinations tend to be roughly the same. For the

one-hidden layer BP network in Fig. 8 (a) and (c), the lowest RMSE is achieved by the combination of logsig + purelin and tansig + purelin, slightly higher RMSE by logsig + tansig and tansig + tansig and much large RMSE by the rest combination of activation functions. The RMSE decreases with the increase of the neuron number for the four better combinations of activation functions above and converges when the neuron number is up to about 15. For the two-hidden-layer BP network in Fig. 8 (b) and (d), the best combinations are observed as logsig + tansig, logsig + logsig, tansig + tansig and tansig + logsig. The purelin + purelin performs the worst, while the other combinations produce slightly worse results compared to the best four combinations. The best four combinations converge when the neuron number is about 9. Based on the RMSE evaluation above, it is easy to conclude that good prediction is achieved by the combinations of logsig + purelin and tansig + purelin for one-hidden-layer networks, and logsig + tansig, logsig + logsig, tansig + tansig and tansig + logsig for two-hidden-layer networks. The following study shows that one-hidden-layer BP network is a good balance between high accuracy and computation efficiency. Besides, one-hidden-layer BP network is simpler than multiple hidden layer network. Therefore, the tansig activation function is used between the input layer and hidden layers, and the purelin activation function is used from the last hidden layer to the output layer for the consistency purpose.

Effect of the number of hidden layers and neurons is studied for the activation function combination of tansig + purelin, as compared in Fig. 9 for the RMSE of the training/testing sets. Fig. 9 (a) shows that RMSE of the training set converges to a stable value faster than that of the testing set for the two-hidden-layer and three-hidden-layer networks. It is observed from the Fig. 9 (b) that the three-hidden-layer network performs better than the one-hidden-layer and two-hidden-layer networks when the neuron number is less than 20. When there are more than 20 neurons in each layer, the RMSE obtained reaches a platform. It is concluded that there is no benefit in increasing the network scale when the number of hidden layers and neurons is large enough. Besides, when the number of hidden layer is fixed, the predicting accuracy increases with the neuron number of each hidden layer. It means that the predicting accuracy can be improved either by raising the number of hidden layers or adding more neurons with less hidden layers. Either approach can reach to very similar accuracy once the neuron number is large enough.

The above conclusion can be further corroborated from the three-dimensional Fig. 10 which shows the predicting accuracy for the two-hidden-layer BP network with different neuron number in each layer. The black line represents the RMSE of the single-hidden-layer network, and the red line represents the RMSE of the two-hidden-layers network. Obviously, the RMSE of the training set reaches to a platform faster than

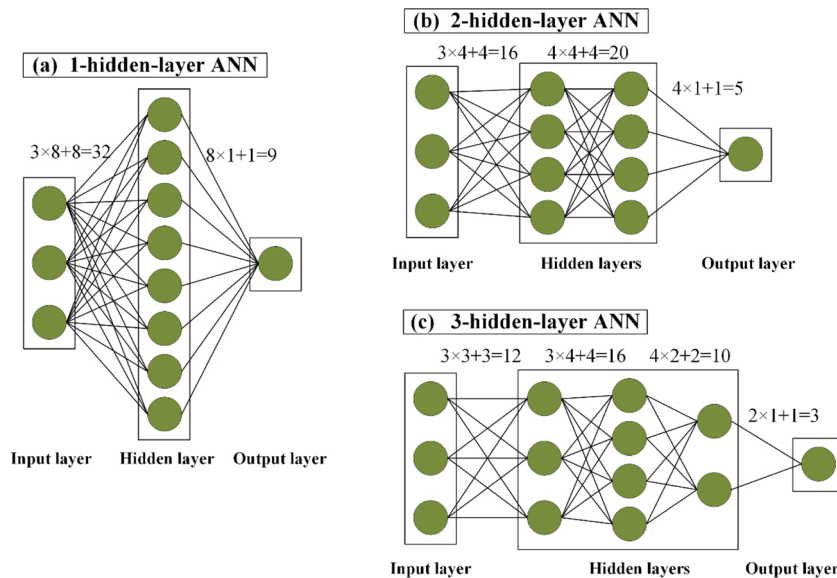


Fig. 11. Schematic of the ANN with the total parameter number of 41 corresponding to (a) single hidden layer; (b) two hidden layers; and (c) three hidden layers.

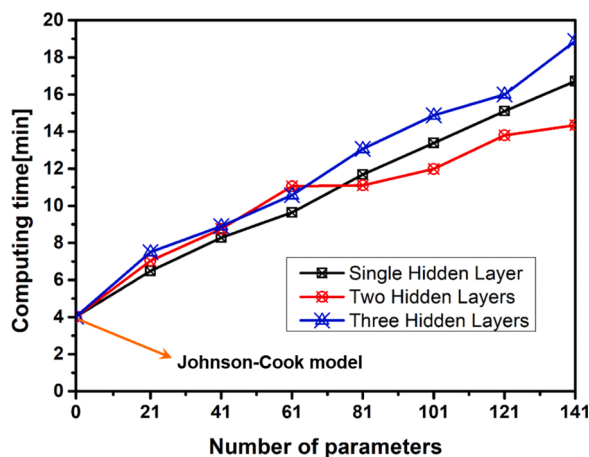


Fig. 12. Finite element calculation time under the same parameters.

the testing set even when the structure of the neural network is relatively simple. There is a little big difference of the predicted RMSE for the training and testing sets even though the trend is very similar with respect to neuron number and the number of hidden layers. The testing set can better reflect the predicting accuracy of the BP network as shown in Fig. 10 (b). According to the observation above, the RMSE gradually decreases with the increase of neuron number, but the adding of new hidden layers does not improve the predicting accuracy of the testing set apparently. Therefore, increasing neuron number is the effective approach to improve the predicting accuracy of the BP network. Besides, a single-hidden-layer BP network is recommended because increasing the number of hidden layers does not improve the predicting accuracy dramatically.

In addition to the predicting accuracy, the computation time of numerical simulation is the other key factor because engineers and scientists would like to get reliable results with short time. Therefore, the computation time of different network structures is compared in term of the parameter number (the sum of weights and thresholds). The prediction performance of the ANN model is tested under three different hidden layer cases. To ensure that the parameter number is identical for different number of hidden layers, different architectures of the ANN

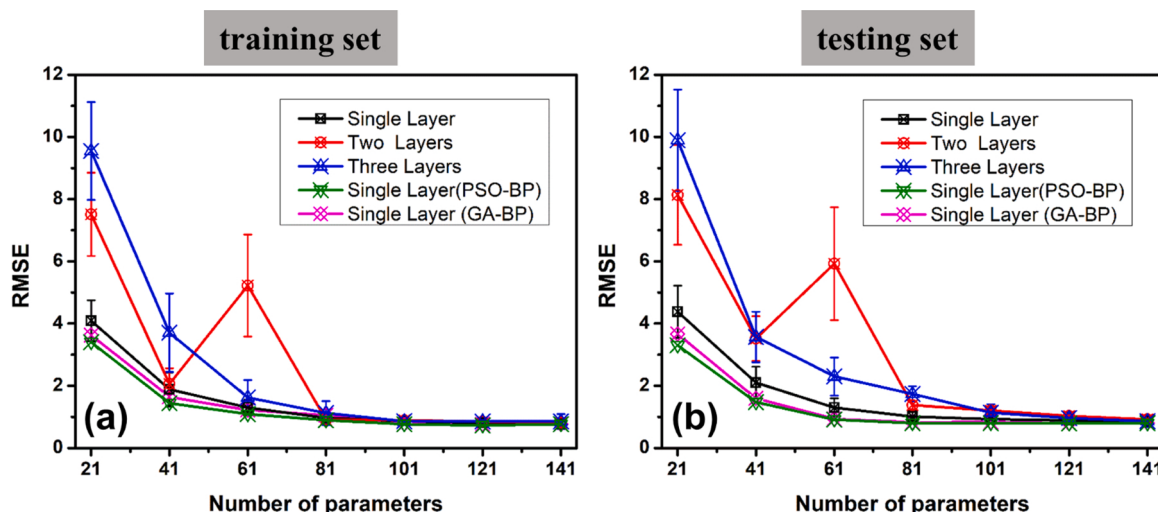


Fig. 13. Comparison of calibration errors under the same number of parameters: (a) training set (b) testing set.

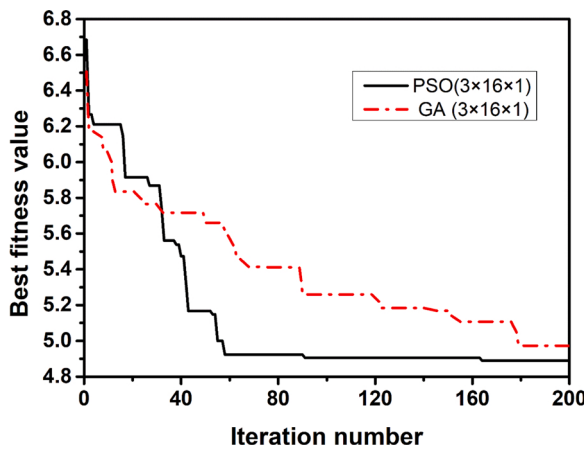


Fig. 14. The plot of best fitness value.

model is constructed for different hidden layers as summarized in Table 2. The ANN model with these architectures has identical number of parameters for different hidden layer number as below: 21, 41, 61, 81, 101, 121 and 141. Taking the 41 parameters as an example, three constructed network structures are shown in Fig. 11 with the computation method of parameter number by summing the connections

between layers and neurons in every layer.

Fig. 12 summarizes the finite element calculation time of neural networks with different parameters. A dogbone experiment at a temperature of 300 K and a strain rate of 0.01 mm/s is simulated on a common performance computer (Intel(R) Core(TM) i7-9700 CPU @ 3.00 GHz 3.00 GHz; 16.0 GB RAM; 4 CPU for all the simulations). The convergence criterion for training is met after 101 epochs. For the comparison purpose, numerical simulation time is also obtained for the JC model which is pointed out at the left hand side in Fig. 12. Its position indicates that the computing time is about four minutes for the JC model. First, it is observed that the structures of neural networks have little effect on the computing time of the neural network if the parameter number is identical for different network structures. Second, the computing time is strongly affected by the parameter number of neural networks. As the parameter number increases, the calculation time of the finite element also linearly increases. Therefore, it is suggested to use an ANN network with less parameters for high computing efficiency. At last, the computing time for ANN model is longer than that with the JC model, which indicates that the ANN model is not computation effective compared with the JC model. The computing time of ANN model is less than two times of the JC model when the ANN parameter number is 21. The ANN computing time rises to about two times for ANN model with 41 parameters, three times for 81-parameter network, and four times for 141-parameter neural network. Accordingly, the network needs to have less number of parameters to raise the computing efficiency.

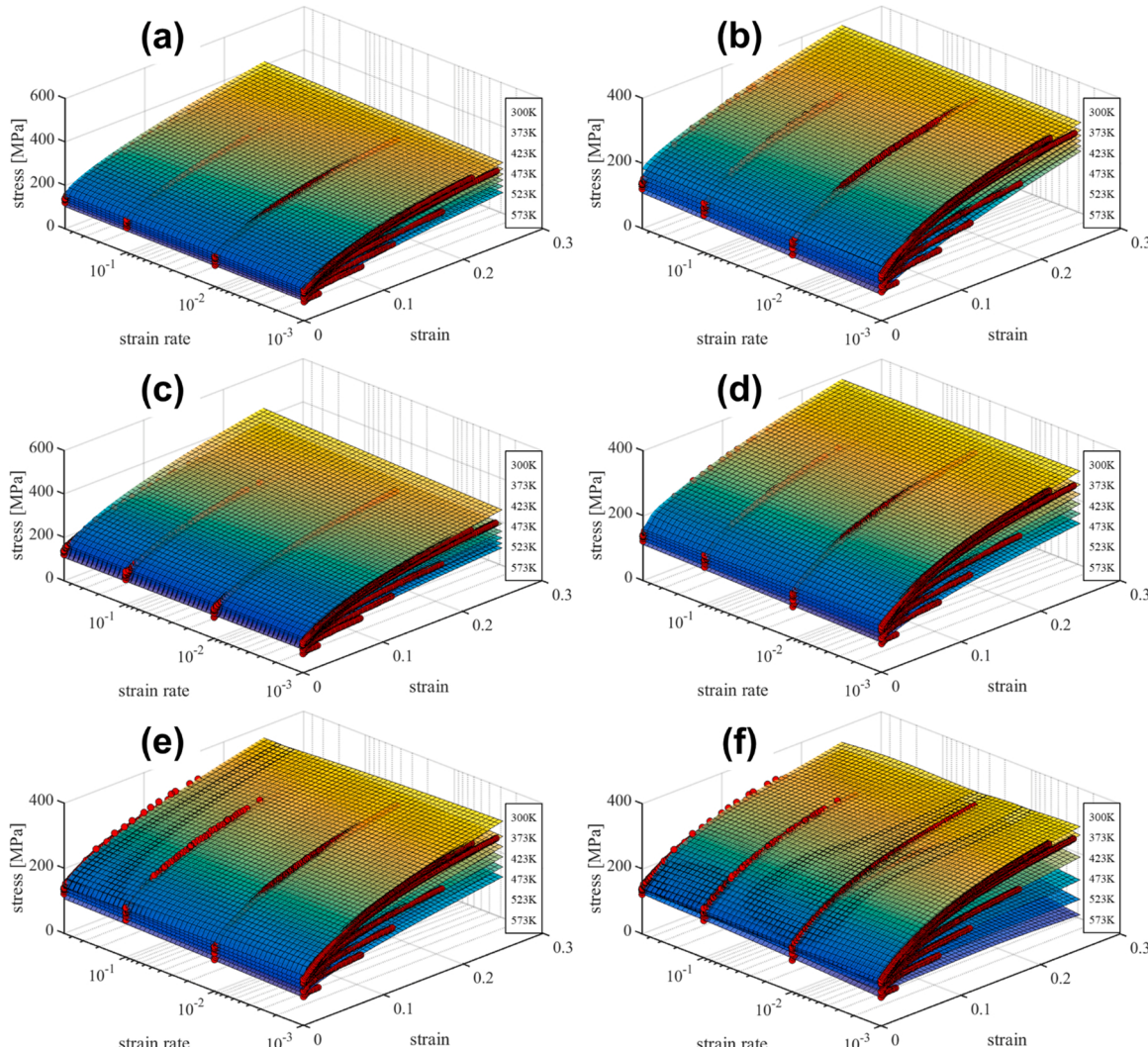


Fig. 15. Comparison between calculated flow stress and experimental data: (a) JC; (b) ZA BCC; (c) ZA FCC; (d) LH; (e) CP; (f) ANN.

Table 3

Material coefficients of constitutive models.

Johnson-Cook (ref. Strain rate: 1 s ⁻¹)									
A	B			n		c		m	
161.96	618.62			0.627		0.016		1.18	
Zerilli-Armstrong for BCC (ref. Strain rate: 1 s ⁻¹)									
C ₀	C ₁	C ₃	C ₄	C ₅				n	
-1785.82	61,446	4.34 × 10 ⁻⁶	1.36 × 10 ⁻⁷	558.76				0.72	
Zerilli-Armstrong for FCC (ref. Strain rate: 1 s ⁻¹)									
C ₀	C ₂	C ₃	C ₄						
106.42	1621	2.8 × 10 ⁻³	7.7 × 10 ⁻⁵						
Lim-Huh model (ref. Strain rate: 0.001 s ⁻¹)									
A	ε_1	n	q ₁	q ₂	q ₃	p ₁	p ₂	p ₃	m ₁
629	0.2784	0.3859	0.0236	-0.0025	0.38	0.001	9.32 × 10 ⁻⁶	1.488	0.997
Coupled polynomial (ref. Strain rate: 0.001 s ⁻¹)									
A	n	B	C	D	E	F	G	m	
0.0242	0.089	0.62	-729.32	6315.57	2709.84	-7.7	-2014	0.98	

Since the computing time increases proportionally with the parameter number of the network as shown in Fig. 12, it makes sense to investigate the effect of parameter number on the predicting accuracy of ANN model. Fig. 13 shows the influence of the parameter number on RMSE for different network structures of different hidden layers in Table 2. It is apparent that the computing error reduces approximately with the parameter number for one-hidden-layer, two-hidden-layer and three-hidden-layer networks. With the same parameter number, the RMSE of the one-hidden layer network is less than those of the two-hidden-layer and three-hidden-layer networks. Considering that the computing time rises with the parameter number, the one-hidden-layer network is better than a network with more hidden layers in term of both predicting accuracy and numerical computation efficiency.

The RMSE of the training and testing sets under the same number of parameters is shown in Fig. 13. The results show that although the difference between the predicting errors of the training and testing sets is not obvious when the parameter number is 21, the predicting errors of different hidden layers of the training set decrease greatly after the parameter is 41. Since the neural network structure is 3-2-13-1 when the parameter is 61, the neurons in the first hidden layer is less than the neurons in the input layer, resulting in the loss of input information and inaccurate prediction results. Fig. 13 (b) shows that the predicting results of testing set under different structures tend to be roughly consistent when the parameter number is up to 81. The comparison demonstrates that the network trained by GA and PSO algorithms predicts with smaller RMSE. The performance of the PSO algorithm is slightly better than the GA algorithm, but the difference is not obvious. The fitness values of the GA and PSO algorithm are also compared in Fig. 14. It is shown that the PSO algorithm has a better fitting effect than the GA algorithm. It indicates that the PSO algorithm accelerates the convergence of a network to the optimal value.

According to the comprehensive analysis of the BP network on the predicting accuracy and computation efficiency for the modeling of strain rate and thermal effect on strain hardening, several conclusions can be drawn as follows:

- (1) The combinations of logsig + purelin and tansig + purelin is suggested to be used for one-hidden-layer networks, and logsig + tansig, logsig + logsig, tansig + tansig and tansig + logsig for two-hidden-layer networks to improve the predicting accuracy of BP networks.
- (2) The predicting error monotonically decreases with the neuron number, but increasing the neuron number cannot dramatically reduce the predicting error when the number is large enough.
- (3) The computing time is mainly affected by the parameter number for networks with different hidden layers.

- (4) For different networks with identical parameter number, the one-hidden-layer network provides better prediction than networks with more hidden layers.
- (5) The GA and PSO algorithms can further improve the predicting accuracy of the one-hidden-layer network with different number of neurons and parameters.

Accordingly, the one-hidden-layer BP network with 16 neurons in the hidden layer denoted by 3 × 16 × 1 in Table 2 is selected as the ANN model to describe the strain rate and thermal effect on the highly nonlinear strain hardening behavior of 5182-O. The selected network has 81 parameters with a good balance between predicting accuracy and computing efficiency as proved in Figs. 12 and 13. The combination of tansig + purelin is used as the activation function for the network. The network is trained by the PSO algorithm with RMSE as 0.792. The computing time is 11.68 min for the uniaxial tensile tests with a strain rate of 0.01/s at 300 K, which is slightly less than three times the calculation time with the JC model. This trained network is compared with JC, ZA, LH and CP models in terms of the analytical and numerical predicting accuracy and numerical computation efficiency in the following sections.

Prediction evaluation of flow curves at different strain rates and temperatures

In order to apparently evaluate the performance of different models on the strain rate and thermal effect on plasticity, Fig. 15 shows the predicted strain rate effect at different temperatures. These models are calibrated by experimental data in Figs. 5 and 6, and the BP neural network with the structure of 3 × 16 × 1 is trained using the PSO algorithm. The calibration parameters are summarized in Table 3 for analytical models. The predicted surfaces are constructed by the calibrated models at each loading temperature with continuous strain and strain rate. The red solid symbols in Fig. 15 represent the experimental results of uniaxial stretching under different conditions of strain rates and temperatures. It is obviously noted that all the models predict correctly the thermal softening effect of the material: rising temperature reduces the load capability of the material. The gap between surfaces predicted by ANN in Fig. 15 (f) is also observed to be much larger than other models at large plastic strain. This indicates that ANN prediction is very similar with the experimental observation in Fig. 6 that thermal softening effect is more apparent at large deformation than the onset of yielding. However, it is difficult to evaluate the prediction of strain rate effect in the 3D representations. For a fixed strain rate and temperature, the resistance to deformation increases with the equivalent plastic strain. In terms of its monotonicity, ANN is similar to other traditional constitutive models. In general, it is worth noting that despite the large range of training data, the surface predicted by ANN is still particularly smooth. Specifically, when there are four orders of magnitude difference in strain rate, ANN does not create additional peaks or

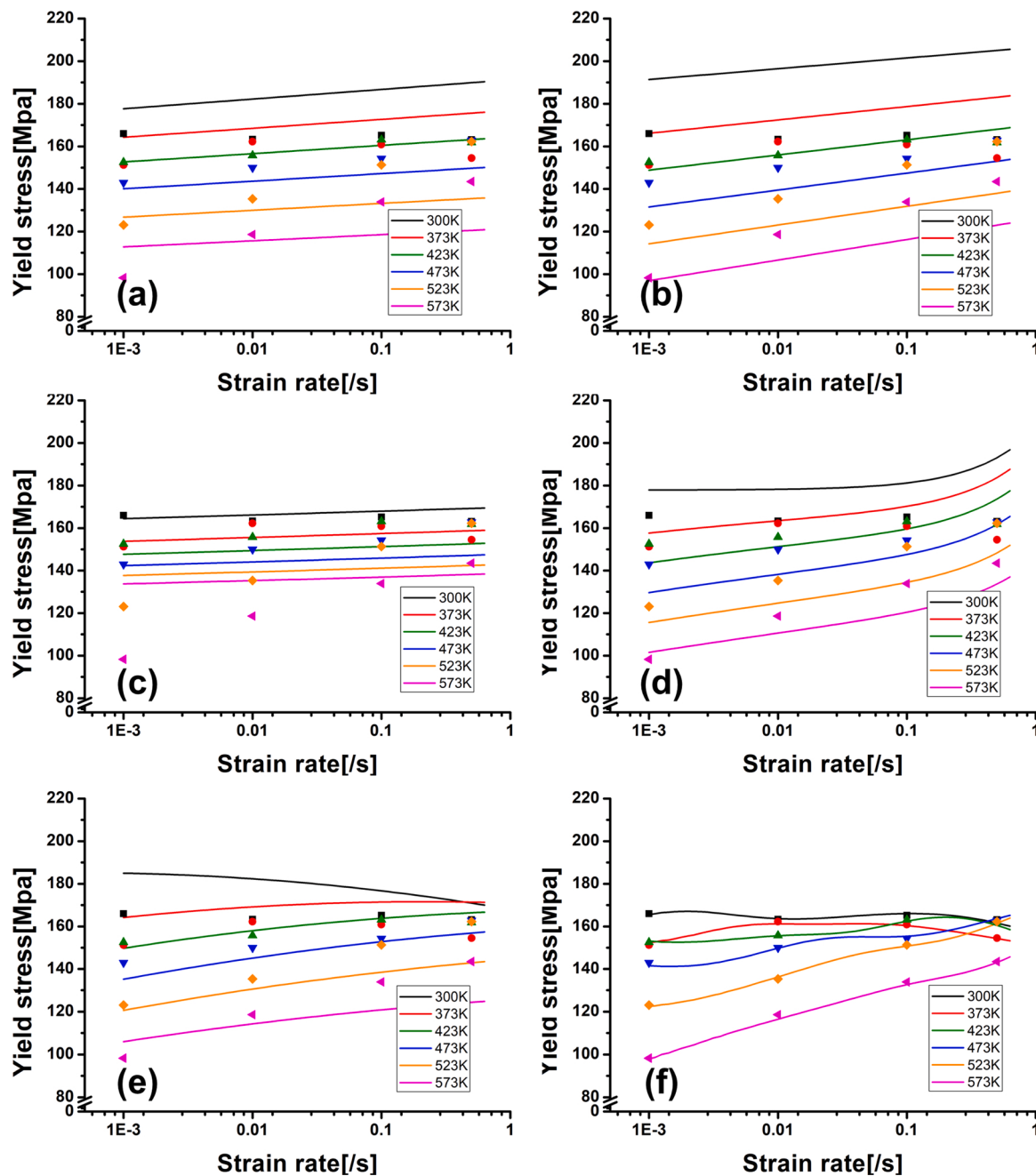


Fig. 16. Comparison between calculated yield stress and experimental data at a plastic strain of 0.01: (a) JC; (b) ZA BCC; (c) ZA FCC; (d) LH; (e) CP; (f) ANN.

valleys in areas which are not covered by the training data.

Since the yield stress indicates the beginning of plastic deformation, it is very important to accurately represent the change in yield stress with respect to strain rate and temperature. Fig. 16 shows the yield stress comparison at a small plastic strain of 0.01. It can be seen from the comparison that all models exhibit a thermal softening effect, which shows that the yield stress decreases with raising temperature. The calibration curves of the JC, ZA BCC and ZA FCC models are approximately parallel with each other at different temperatures. The predicted yield stress increases with strain rate with little change in the slope for these three models. The two observations indicate that a positive strain rate is modeled by these three models, but the modeled strain rate effect does not change much with strain rate and temperature. These observations are contradictory with experimental results that the strain rate effect is negative at 300 K and positive at high temperature. The contradictory observation reveals that these three models cannot describe

the change of strain rate effect with respect to different loading temperatures.

The predicted yield stress at 0.01 plastic strain is compared with experimental results for the LH model in Fig. 16 (d). It is observed that the difference between the predicted yield stress of different temperatures reduces with the increase of strain rate, which is similar with experimental observation. Besides, the predicted strain rate effect is all positive for different temperatures, but experiments show negative strain rate at 300 K. The predicted strain rate hardening is also noted to be higher at high strain rate, but experiments show that strain rate hardening is approximated linear with respect to strain rate. Compared with the JC, ZA BCC and ZA FCC models, the LH prediction is much closer to experimental results even though there are still some contradictory observations between experiments and the LH prediction.

The proposed CP model in Eq. (1) predicts the yield stress at 0.01 plastic strain as compared with experimental results in Fig. 16 (e). It is

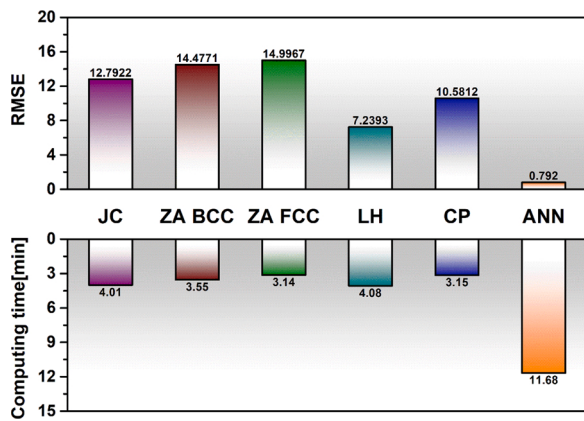


Fig. 17. RMSE and computing time of different models.

observed that negative strain rate effect is modeled by the CP model at 300 K and positive strain rate effect is predicted for higher temperature. This observation is similar with experimental results. The prediction is also observed to be more accurate than the JC, ZA BCC and ZA FCC models, but large gaps are still noted between predictions and experimental data points.

The strain rate effect predicted by the trained ANN model is compared with experiments at different temperatures at 0.01 plastic strain in Fig. 16 (f). It is apparent that the slightly negative strain rate effect is correctly modeled by the ANN model at room and low temperature. When the temperature is equal or higher than 423 K, a positive strain rate effect is modeled and the positive strain rate effect is more apparent as temperature rises. The prediction of the ANN is almost perfectly consistent with the experimental data. The predicted accuracy is apparently much higher than the all the other models.

To further evaluate the predicting accuracy of all the analytical models and the ANN model, the RMSE of the whole data set is computed by Eq. (13) and compared in Fig. 17. First, the ZA BCC and ZA FCC models are less accurate than the JC model considering that the RMSE of the JC model is less than those of the ZA BCC and ZA FCC models. Second, it is observed that the LH model is much more accurate than the JC, ZA BCC and ZA FCC models since the RMSE is just 7.2393 for LH, which is much lower than the other three models. Third, the proposed CP model in Eq. (1) performs much better than the JC, ZA BCC and ZA FCC models since its RMSE is just 10.5812. However, the accuracy of the CP model is lower than the LH model even though the CP model can model the strain rate effect changing from negative at room temperature to positive at elevated temperature. At last, the RMSE of the ANN prediction is just 0.792, which is less than 1/10 of the JC, ZA BCC, ZA FCC and CP models, and about 1/9 of the LH model. The accuracy of the ANN model is unbelievably higher compared with other models.

In addition to the predicting accuracy, the computation efficiency is also compared between different models. All the models are implemented into ABAQUS/Explicit by preparing VUMAT codes. Uniaxial tensile tests are simulated at 300 K with a strain rate of 0.01/s with calibrated parameters in Table 3. The numerical simulation time is also compared in Fig. 17. The computing efficiency in the ascending order is ZA FCC, CP, ZA BCC, JC, LH and ANN. There is very little difference between ZA FCC and CP models, for which it takes 3.14 min and 3.15 min, respectively. Both of the models are more computing effective than the other models. Considering that the predicting error of the CP model is much lower than the JC, ZA BCC and ZA FCC models, the proposed CP model is suggested to be used rather these three models. The LH model takes 4.08 min for the simulation, which is slightly higher than all the other analytical models, but its accuracy is the highest among them. It takes 11.68 min for the ANN model with the 3-16-1 structure, which is the longest among all the models. However, considering the highest accuracy of the ANN model, it is worthy spending long time for more

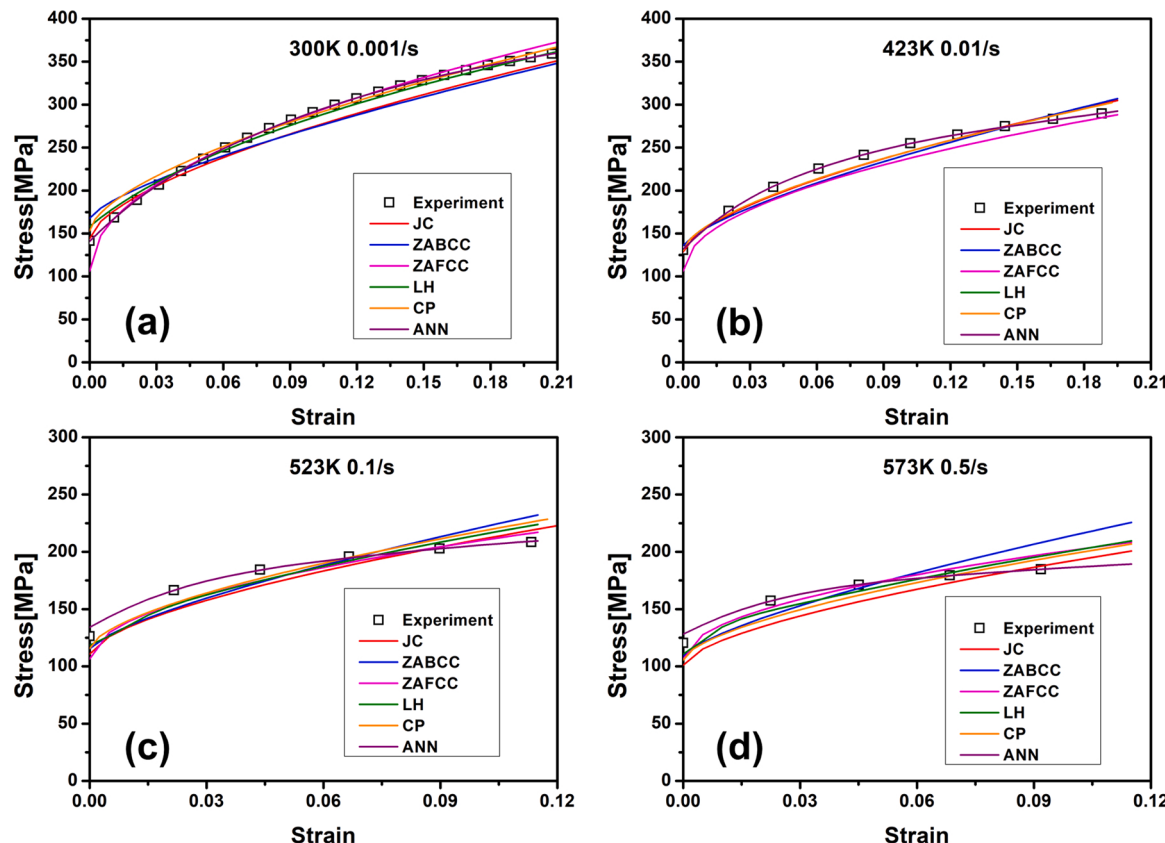


Fig. 18. Comparison of prediction accuracy on flow curves for (a) 300 K-0.001/s, (b) 423 K-0.01/s, (c) 523 K-0.1/s, (d) 573 K-0.5/s.

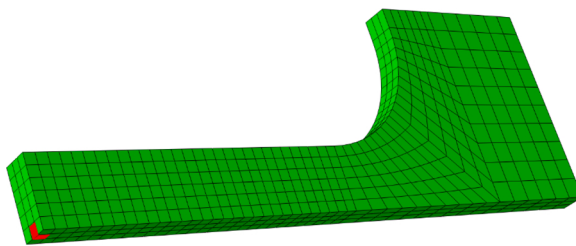


Fig. 19. Detailed solid element meshes of dogbone specimen.

reliable numerical analysis especially for the era of rocketing computation power with reduced cost.

Due to limited space, the predicted flow curves by all the models are compared with experimental measurement of four representative results in Fig. 18 (a) for 300 K-0.001/s, (b) for 423 K-0.01/s, (c) for 523 K-0.1/s, and (d) for 573 K-0.5/s. It is found that the calibration results of all the models are roughly the same except for the ANN model. The prediction results of the ANN model approximately overlap with the experimental curves for these four loading conditions. The predicting accuracy by the

ANN model is also observed very high for the rest 20 loading conditions at different loading conditions, but the comparison is not included in the text due to limited length.

Numerical prediction of load-stroke curves

The JC, ZA, LH, CP hardening functions and ANN model are implemented in ABAQUS user material subroutines (ABAQUS/Explicit VUMATs). It is worth pointing out that to verify the accuracy of VUMAT development for different loading conditions, the simulation results are compared between the developed JC subroutine and the built-in JC constitutive function in ABAQUS. The comparison proves that our models are implemented correctly. The reaction forces are predicted for the tension of dogbone specimens by all the models with the calibrated parameters in Table 3. Fig. 19 shows the detailed finite element mesh of the specimen used. A quarter symmetric model is adopted with symmetric boundary conditions to save running time. For thermal-mechanical finite element simulation, the following thermal constants are determined: the thermal expansion coefficient is $2.3 \times 10^{-5}/\text{K}$, the specific heat capacity is 904 J/kg·K and the thermal conductivity is 220 J/m K (Abedrabbo et al., 2007). During the deformation process, part of the plastic work is converted into heat, and the rest is stored elastically or

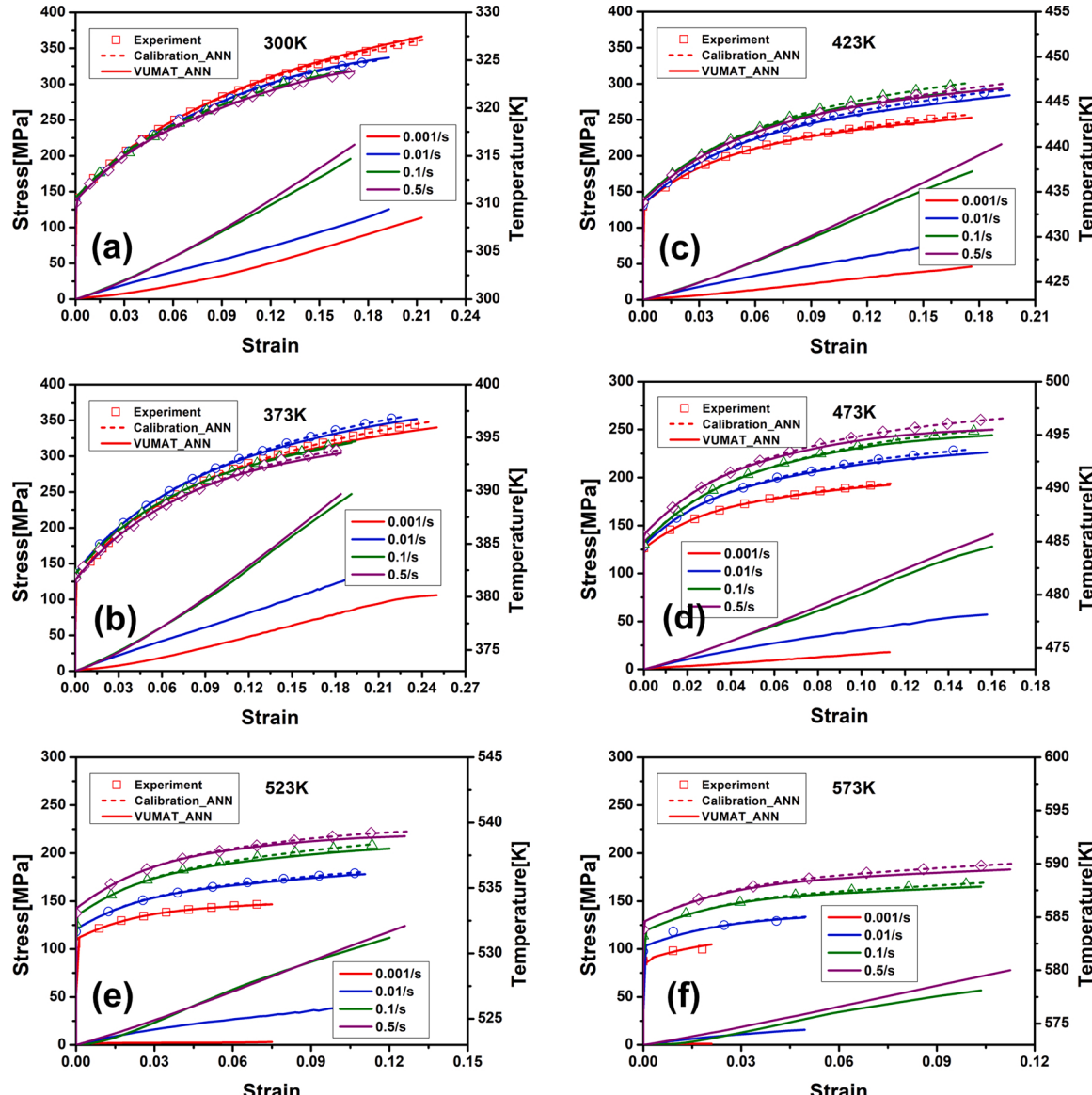


Fig. 20. Calibration of hardening curve (ANN) for (a) 300 K, (b) 373 K, (c) 423 K, (d) 473 K, (e) 523 K and (f) 573 K.

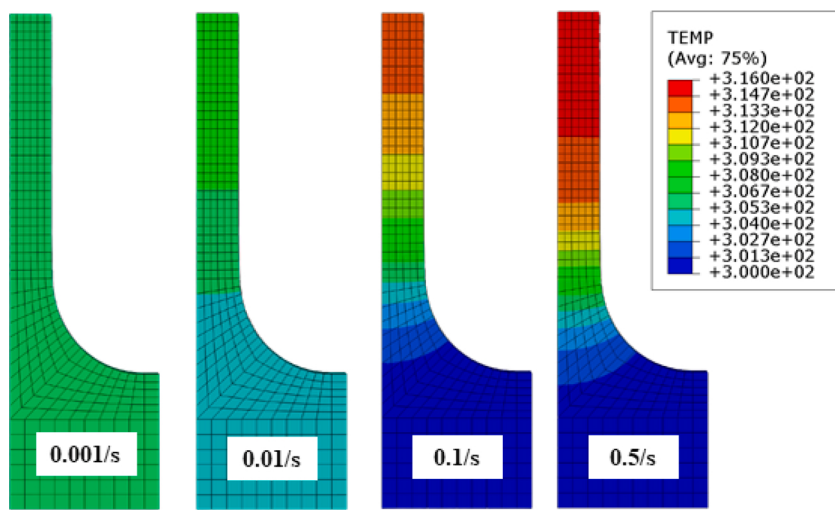


Fig. 21. Temperature distribution of tests at 300 K for different strain rates (a) 0.001/s, (b) 0.01/s, (c) 0.1/s and (d) 0.5/s.

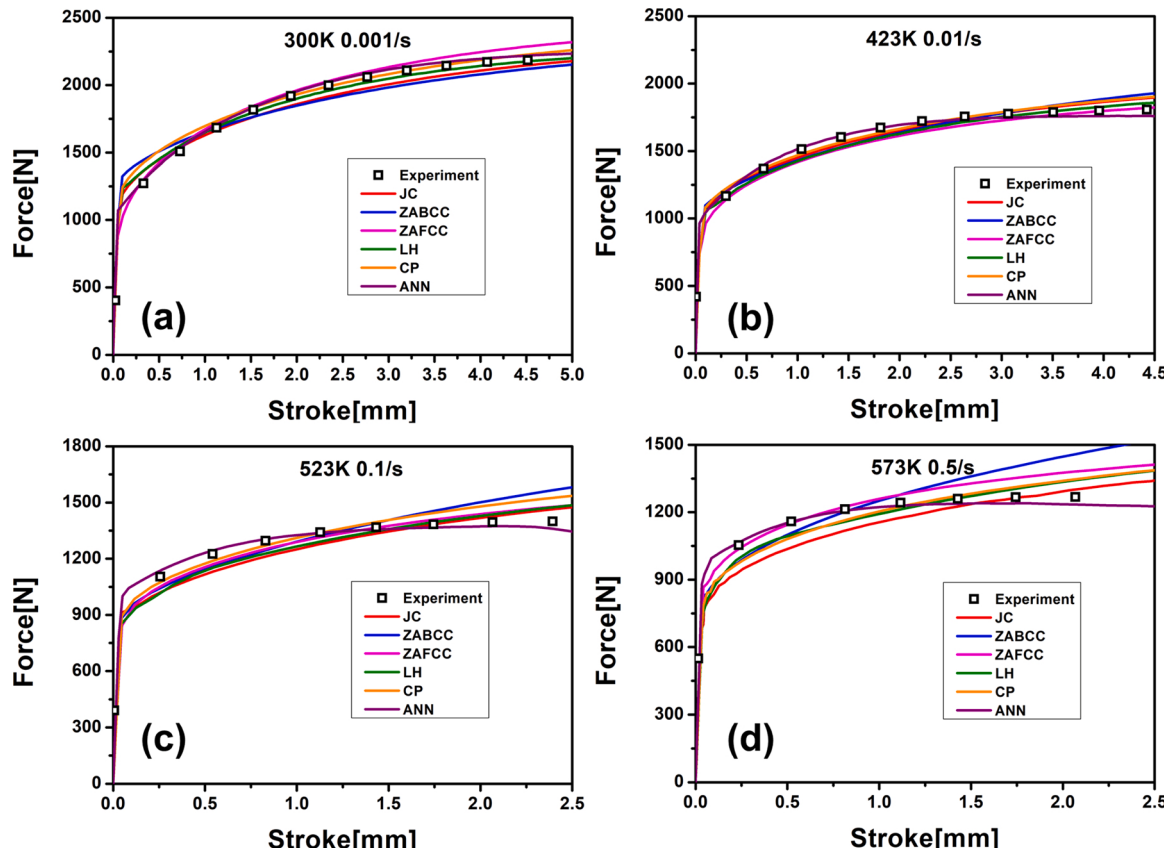


Fig. 22. Comparison of finite element results of different constitutive models with dogbone specimen experiments: (a) 300 K-0.001/s, (b) 423 K-0.01/s, (c) 523 K-0.1/s, (d) 573 K-0.5/s.

consumed by plastic deformation. Here, the thermal conversion rate of plastic deformation is set to 0.9 (Sung et al., 2010). The von Mises yield function and the law of isotropic hardening are adopted due to the path of the uniaxial tensile stress is almost proportional throughout the test.

The flow curves and temperature increase are extracted from numerical simulations by the ANN model for the element at the center of the specimen highlighted in red in Fig. 19. The extracted flow curves are compared with experimental results and the analytical prediction by the ANN model in Fig. 20 for 21 loading conditions of different strain rates and temperatures. Fig. 20 (a) shows that the ANN model can accurately

represent the negative strain rate effect of 5182-O at 300 K. In Fig. 20 (b) for tests at 373 K, the strain rate effect is positive from 0.001/s to 0.01/s and turns to be negative from 0.01/s to 0.5/s. The changing of strain rate effect is correctly modeled by the ANN model for this case. At 423 K, the strain rate effect is positive from 0.001/s to 0.1/s and then becomes negative beyond 0.1/s, as shown in Fig. 20 (c). This complex strain rate effect is also accurately modeled by the ANN model. When testing temperature is higher than or equal to 473 K, the strain rate effect is all positive and the positive strain rate effect is more apparent for higher temperatures, as observed in Fig. 21 (d), (e) and (f). The effect at the

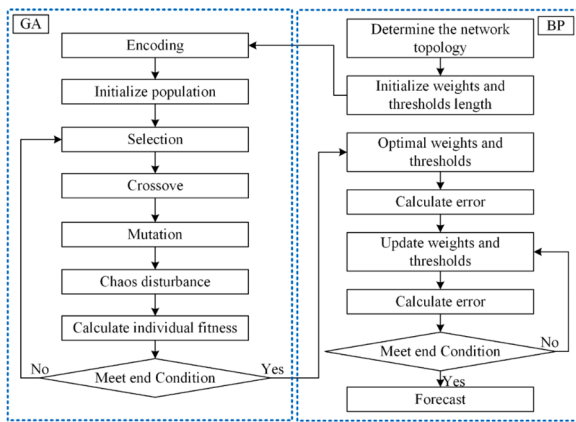


Fig. C1. GA-BP calculation process.

high temperatures is all predicted with good agreement by the ANN model. The comparison reveals that analytically, the ANN model accurately describes the nonlinear coupling effect of thermal softening and strain rate hardening with wide range of temperature from 300 K to 573 K.

However, the flow curves analytically predicted by the ANN model are slightly different from the numerical simulation results as shown in Fig. 20. It is because in numerical simulation, there is some amount of temperature increase and strain rate changing due to the elongation of stretching gauge. In analytical prediction, the strain rate and temperature are assumed to be constant. The difference is also noted to be magnified at large strain because large plastic strain induces higher temperature increase. Besides, temperature increase is higher for high strain rate, which causes significantly lower flow curves at high strain rates in numerical simulation by ANN than analytical prediction. It is because temperature rise is much higher for high strain rate considering that time is limited for thermal conduction at high strain rate. This can also be confirmed in Fig. 21 which shows the temperature distribution of the tests under 300 k at a stroke of 3.5 mm.

The force-displacement curves are numerically predicted for the tension of the dogbone specimen by all the models of JC, ZA BCC, ZA FCC, LH, CP and ANN at 24 loading conditions. In order to echo the results in Fig. 18, the predicted curves are compared with experimental results in Fig. 22 (a) for 300 K-0.001/s, (b) for 423 K-0.01/s, (c) for 523 K-0.1/s, and (d) for 573 K-0.5/s. It is obvious that only the ANN model predicts the reaction force with much better agreement compared with experimental results for the tensile tests with a strain rate of 0.01/s at 300 K. The prediction of all the other models cannot reasonably describe the strain rate effect of the material at 300 K. The remaining three sets of results demonstrate that the ANN model can accurately predict the reaction force at high temperatures, while the JC, ZA BCC, ZA FCC, LH and CP models predict the reaction force of these loading conditions with

poor accuracy. Besides, the predicted force by the ANN model is slightly lower than the experimental one at large strain especially at high strain rate. This is because in the numerical simulation, there is temperature increase due to plastic deformation especially for high strain rate as shown in Figs. 20 and 21, while it is assumed that temperature is constant during tensile tests during the calculation of flow curves by the force-displacement curves. The plastic deformation induced temperature increase attributes to the lower prediction of reaction force at large deformation by thermal softening effect.

In summary, it can be seen that the prediction results of the ANN model are significantly better than the traditional constitutive models. The theoretical calibration results by ANN model are perfectly consistent with the experimental results, but the simulation results are slightly lower than the theoretical calibration results at large strain. This is because the plastic deformation induced temperature increase is coupled in numerical simulation, while it is neglected during analytical calculation of flow curves. Compared with other models, the ANN model is the best in accuracy for coupling effect of 5182-O.

The purpose of this study is to characterize and simulate the dynamic hardening behavior of 5182-O. After the parameters of the constitutive model are calibrated by the experimental data, the traditional constitutive models and the ANN model are applied to the finite element subroutine. The calibration results of each model are quantitatively compared by RMSE. It can be found that the prediction error of the ZA FCC model reaches 14.9967, which is the worst in accuracy. The model with the highest prediction accuracy among the traditional models is the LH model, with an error of 7.2393. The proposed CP model can model the changing strain rate effect with testing temperature, provide better accuracy than all traditional models except the LH model. Besides the numerical computation efficiency by the CP model is the highest among the models. As to the ANN model, its prediction error is only 0.792 which is dramatically lower than all the other models. The results show that the ANN model can accurately capture the coupled effect of strain rate and temperature, while the traditional constitutive models cannot. Moreover, the single-layer ANN model optimized by the PSO algorithm not only has excellent calibration accuracy, but also the calculation time of the finite element is within the acceptable range. In summary, it can be concluded from the current research that the ANN model is an emerging phenomenological model, which accurately describes the dynamic hardening characteristics of 5182-O considering the coupling effect during warm forming.

7. Conclusions

This research studies the dynamic hardening behavior of 5182-O including comprehensive experiments, analytical and ANN modeling and numerical prediction of reaction forces at different loading conditions. This study leads to following conclusions:

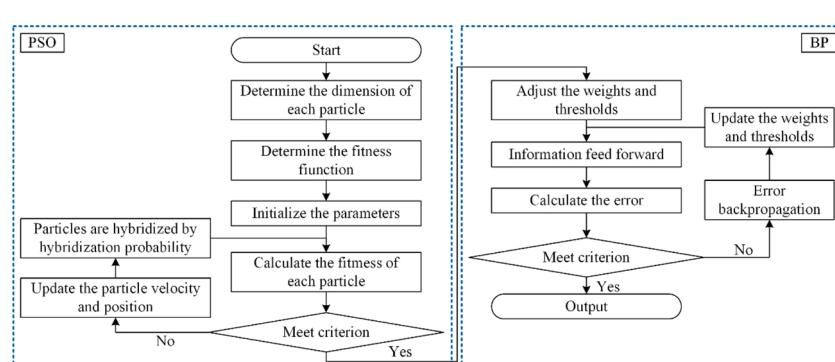


Fig. C2. PSO-BP calculation process.

- (1) The experiments show that the strain hardening behavior is very complicated. The strain rate and thermal effect is strongly coupled. Strain rate effect is slightly negative at 300 K. As the loading temperature rises, the strain rate effect turns to be positive and the positive strain rate effect becomes stronger with temperature.
- (2) The strong coupled effect of strain rate and temperature cannot be modeled by conventional models which treat the strain hardening, strain rate hardening and thermal softening independently.
- (3) The proposed CP model takes into account the coupled effect of strain rate and thermal softening. The comparison with experiments and numerical simulation show that the CP model predicts the strain hardening at different strain rates and temperatures with better accuracy than the conventional JC and ZA models, and the computation efficiency of the CP model is also higher than the JC, ZA BCC and LH models. Therefore, the proposed CP model is a good option to model the highly coupled effect considering its high accuracy and computation efficiency.
- (4) The BP network is also applied to model the coupled effect and numerical simulation of dogbone tension at different loading conditions. Parameters of the BP network are comprehensively investigated on the prediction accuracy. To achieve high prediction accuracy with short numerical simulation time, the following BP network is suggested: one hidden layer with logsig + purelin or tansig + purelin as activation functions. The PSO algorithm is recommended to be used to train the BP network to fully achieve the high predicting accuracy potential.
- (5) The computation efficiency is observed to be strongly affected by the parameter number of the BP network with different hidden layers. The numerical simulation time increases proportionally with parameter number. Therefore, a BP network with less parameters is preferred considering the numerical computation time.
- (6) The numerical prediction by analytical models and BP network proves that the BP network greatly improves the predicting accuracy of reaction forces at different loading conditions, even though the computing time is somewhat longer than the analytical models. The reduced computation efficiency is worth considering the great enhancement of prediction accuracy by the ANN model compared with the conventional models.

This study shows that the machine learning-based model can precisely predict the strongly coupled effect on the dynamic hardening behavior of 5182-O. However, there are still many questions and limitations which can be further studied. These questions cannot be answered due to the length of the research, and the limitations are not properly solved currently. Some limitations are listed as below for further improvement of this study:

- (1) The performance of the neural network needs to be further verified by other types of experiments and application in high temperature stamping of the alloy.
- (2) The trained ANN is expected to perform with high accuracy when the deformation is less than necking strain, the strain rate between 0.001/s and 0.5/s and the temperature from 300 K to 573 K. It is because the ANN is trained by experiments of these loading conditions. However, its applicability is questioned beyond the range.
- (3) The strain hardening needs to be reasonably characterized by experiments at large strain beyond necking since the fracture strain is much higher than the necking strain at high temperature under uniaxial tension. The hardening behavior up to large strain is key to extend the application of the ANN model for high temperature forming of the alloy.

Data availability

We have reviewed published papers, most of which have not yet made their raw EEG data available.

Data will be made available on request.

Author agreement

We declare that this manuscript entitled "Machine learning-based modeling of the coupling effect of strain rate and temperature on strain hardening for 5182-O aluminum alloy" is original, has not been published before and is not currently being considered for publication elsewhere.

We confirm that the manuscript has been read and approved by all named authors and that there are no other persons who satisfied the criteria for authorship but are not listed. We further confirm that the order of authors listed in the manuscript has been approved by all of us.

We understand that the Corresponding Author is the sole contact for the Editorial process. He is responsible for communicating with the other authors about progress, submissions of revisions and final approval of proofs.

Declaration of Competing Interest

We declare that we do not have any commercial or associative interest that represents a conflict of interest in connection with the work submitted

Acknowledgements

The authors also acknowledge the financial supports by the National Natural Science Foundation of China (Grant No. 52075423), the State Key Laboratory of Mechanical System and Vibration (Grant No. MSV202009), and the State Key Laboratory of High Performance Complex Manufacturing (Grant No. Kfkt2019-02).

Appendix A. Calculation of partial derivatives of LH equation

Constitutive equation of LH reads as

$$\sigma_{(\varepsilon, \dot{\varepsilon}, T)} = [\sigma_r(\varepsilon)] \cdot [\sigma_e(\varepsilon, \dot{\varepsilon})] \cdot [\sigma_T(T, \dot{\varepsilon})] = A(\varepsilon + \varepsilon_0)^n \cdot \left[\frac{1 + q(\varepsilon) \dot{\varepsilon}^{p(\varepsilon)}}{1 + q(\varepsilon) \dot{\varepsilon}_r^{p(\varepsilon)}} \right] \cdot \left[1 - \left(\frac{T - T_r}{T_m - T_r} \right)^{m(\dot{\varepsilon})} \right]$$

where $q(\varepsilon) = \frac{q_1}{(\varepsilon + q_2)^{q_3}}$, $p(\varepsilon) = \frac{p_1}{(\varepsilon + p_2)^{p_3}}$, $m(\dot{\varepsilon}) = m_1 + m_2 \cdot \ln \frac{\dot{\varepsilon}}{\dot{\varepsilon}_r}$, $\dot{\varepsilon} > \dot{\varepsilon}_r$ and $T_r \leq T \leq T_m$.

ε and $\dot{\varepsilon}$ have such a relationship :

$$\frac{d\sigma}{d\varepsilon} = \frac{d\sigma}{d\dot{\varepsilon}} \frac{d\dot{\varepsilon}}{d\varepsilon} = \frac{d\sigma}{d\dot{\varepsilon}} \cdot dt$$

So the partial derivative we get is:

$$\frac{d[\sigma_{(\varepsilon, \dot{\varepsilon}, T)}]}{d\varepsilon} = \frac{d[\sigma_r(\varepsilon)]}{d\varepsilon} \cdot [\sigma_{\dot{\varepsilon}}(\varepsilon, \dot{\varepsilon})] \cdot [\sigma_T(T, \dot{\varepsilon})] + \frac{d[\sigma_{\dot{\varepsilon}}(\varepsilon, \dot{\varepsilon})]}{d\varepsilon} \cdot [\sigma_r(\varepsilon)] \cdot [\sigma_T(T, \dot{\varepsilon})]$$

$$+ \frac{d[\sigma_T(T, \dot{\varepsilon})]}{d\varepsilon} \cdot [\sigma_r(\varepsilon)] \cdot [\sigma_{\dot{\varepsilon}}(\varepsilon, \dot{\varepsilon})]$$

The first partial derivative expression:

$$\frac{d[\sigma_r(\varepsilon)]}{d\varepsilon} = A \cdot n \cdot \varepsilon$$

The second partial derivative expression:

$$\frac{d[\sigma_{\dot{\varepsilon}}(\varepsilon, \dot{\varepsilon})]}{d\varepsilon} = \frac{(1 + q(\varepsilon)\dot{\varepsilon}^{p(\varepsilon)})' \cdot (1 + q(\varepsilon)\dot{\varepsilon}_r^{p(\varepsilon)}) - (1 + q(\varepsilon)\dot{\varepsilon}^{p(\varepsilon)}) \cdot (1 + q(\varepsilon)\dot{\varepsilon}_r^{p(\varepsilon)})'}{(1 + q(\varepsilon)\dot{\varepsilon}_r^{p(\varepsilon)})^2}$$

where

$$(1 + q(\varepsilon)\dot{\varepsilon}^{p(\varepsilon)})' = [-q_1 q_3 \cdot (\varepsilon + q_2)^{-q_3-1}] \cdot \left[\dot{\varepsilon}^{\frac{p_1}{(\varepsilon+p_2)^{p_3}}} \right]$$

$$+ \left[q_3 \cdot \frac{q_1}{(\varepsilon + q_2)} \right] \cdot \left[\dot{\varepsilon}^{\frac{p_1}{(\varepsilon+p_2)^{p_3}}} \cdot \left[(-p_1 p_3) \cdot (\varepsilon + p_2)^{-p_3-1} \cdot \ln \dot{\varepsilon} \right] + \left[\frac{p_1}{(\varepsilon + p_2)^{p_3}} \cdot \frac{1}{\dot{\varepsilon} \cdot dt} \right] \right]$$

$$(1 + q(\varepsilon)\dot{\varepsilon}_r^{p(\varepsilon)})' = [-q_1 q_3 \cdot (\varepsilon + q_2)^{-q_3-1}] \cdot \left[\dot{\varepsilon}_r^{\frac{p_1}{(\varepsilon+p_2)^{p_3}}} \right] + \left[\dot{\varepsilon}_r^{\frac{p_1}{(\varepsilon+p_2)^{p_3}}} \cdot \ln(\dot{\varepsilon}_r) \cdot (-p_1 p_3) \cdot (\varepsilon + p_2)^{-p_3-1} \right]$$

The third partial derivative expression:

$$\frac{d[\sigma_T(T, \dot{\varepsilon})]}{d\varepsilon} = \left(\frac{T - T_r}{T_m - T_r} \right)^{m(\dot{\varepsilon})} \cdot \ln \left(\frac{T - T_r}{T_m - T_r} \right) \cdot \frac{m_2}{\dot{\varepsilon}} \cdot \frac{1}{dt}$$

Appendix B. Constitutive model

Many constitutive models have been proposed to describe strain rate sensitivity and thermal softening. This section lists these equations briefly. In the following expressions: σ is the equivalent flow stress, ε is the equivalent plastic strain, $\dot{\varepsilon}$ is the true strain rate and T , T_r and T_m are absolute, reference and melting temperatures.

- B.1. Johnson-Cook model (Johnson and Cook, 1983)**

$$\sigma(\varepsilon, \dot{\varepsilon}, T) = [\sigma_r(\varepsilon)] \cdot [\sigma_{\dot{\varepsilon}}(\dot{\varepsilon})] \cdot [\sigma_T(T)] = [A + B(\varepsilon)^n] \cdot \left[1 + \text{Cln} \frac{\dot{\varepsilon}}{\dot{\varepsilon}_0} \right] \cdot \left[1 - \left(\frac{T - T_r}{T_m - T_r} \right)^m \right] \quad (\text{B.1})$$

where $\dot{\varepsilon}/\dot{\varepsilon}_0$ is the dimensionless plastic strain rate with $\dot{\varepsilon}_0 = 1\text{s}^{-1}$ ($\dot{\varepsilon}$ is the true strain rate, $\dot{\varepsilon}_0$ is the reference strain rate). Five constants are adopted as A , B , n , C and m . The disadvantage of this model is that it assumes that σ is independently affected by strain, strain rate and temperature.

- B.2. Zerilli-Armstrong model (Zerilli and Armstrong, 1987)**

$$\sigma = C_0 + \left[C_1 + C_2 \sqrt{\varepsilon} \right] \exp[-C_3 T + C_4 T \ln \dot{\varepsilon}] + C_5 \varepsilon^n \quad (\text{B.2})$$

For BCC, ($C_2 = 0$) : $\sigma = C_0 + C_1 \exp(-C_3 T + C_4 T \ln \dot{\varepsilon}) + C_5 \varepsilon^n$

For FCC, ($C_1 = C_5 = 0$) : $\sigma = C_0 + C_2 \varepsilon^{-1/2} \exp(-C_3 T + C_4 T \ln \dot{\varepsilon})$

where C_0 , C_1 , C_2 , C_3 , C_4 , C_5 and n are the material constants. The shortcomings of either model can be observed in the two expressions. For the ZA FCC constitutive model, the yield stress at zero plastic strain does not change with strain rate and temperature. For the ZA BCC constitutive model, the strain hardening factors C_5 and n do not couple the effects of strain rate hardening and temperature softening.

- B.3. Lim-Huh model (Huh et al., 2014)**

$$\sigma_{(\varepsilon, \dot{\varepsilon}, T)} = [\sigma_r(\varepsilon)] \cdot [\sigma_{\dot{\varepsilon}}(\varepsilon, \dot{\varepsilon})] \cdot [\sigma_T(T, \dot{\varepsilon})] = A(\varepsilon + \varepsilon_0)^n \cdot \left[\frac{1 + q(\varepsilon)\dot{\varepsilon}^{p(\varepsilon)}}{1 + q(\varepsilon)\dot{\varepsilon}_r^{p(\varepsilon)}} \right] \cdot \left[1 - \left(\frac{T - T_r}{T_m - T_r} \right)^{m(\dot{\varepsilon})} \right] \quad (\text{B.3})$$

where $q(\varepsilon) = \frac{q_1}{(\varepsilon + q_2)^{q_3}}$, $p(\varepsilon) = \frac{p_1}{(\varepsilon + p_2)^{p_3}}$, $m(\dot{\varepsilon}) = m_1 + m_2 \cdot \ln \frac{\dot{\varepsilon}}{\dot{\varepsilon}_r}$, $\dot{\varepsilon} > \dot{\varepsilon}_r$ and $T_r \leq T \leq T_m$

The first term expresses hardening effect with A , ε_0 and n as strain hardening coefficients. The second term signifies the strain rate effect, where q_1 , q_3 , p_1 , p_2 and p_3 are the strain rate hardening coefficients. The last term is thermal softening term involving rate effect, where m_1 and m_2 represent

the thermal softening behavior.

Appendix C. Optimization algorithm

C.1 BP neural network optimized by genetic algorithm (GA)

GA has good global search performance because it simulates an adaptive iterative optimization process. Here GA is used to optimize the initial weights and thresholds, and the search is performed in a larger range instead of the random selection. In this way, the fitness value is calculated, and the optimal individual is found through selection, crossover and mutation operations. Then the BP algorithm adjusts the neural network parameters to search for the optimal solution. This realizes the extensively nonlinear mapping capabilities of the neural network and the global search capabilities of GA. Moreover, the learning speed of the neural network is accelerated by GA, and even the approximation ability and generalization ability are improved in the whole learning process. The process of BP neural network trained by GA is as follows:

- Step 1. Code and initialize the population

The BP neural network in this research has three layers. Suppose that the number of neurons in the input layer is i , the number of neurons in the output layer is j , and the number of neurons in the hidden layer is n_h . The weights and thresholds corresponding to the hidden layer and output layer of the network are w_1 , w_2 , b_1 and b_2 . The length of the code is $i \times n_h + n_h \times j + n_h + j$.

- Step 2. Fitness function

The GA searches based on the fitness value of each chromosome in the population. Individuals with lower fitness have a relatively smaller probability of inheriting to the next generation. MSE is used to evaluate the capabilities of BP neural networks. In this study, the reciprocal of the MSE is used as the fitness function as follows:

$$f(i) = 1/MSE_i \quad (C.1)$$

- Step 3. Selection

Here the ranking method is used as the selection mechanism to arrange the order according to the difference of fitness value. The selection mechanism is that the greater the fitness value, the greater the probability of being selected. It is sorted in ascending order according to the fitness value, and then the selection probability is calculated according to Eq. (C.2) below:

$$P_i = q' (1 - P_{\max})^{n(i)-1} \text{ with } q' = \frac{P_{\max}}{1 - (1 - P_{\max})^L} \quad (C.2)$$

where P_{\max} is the selection probability of the best chromosome. Then each body is selected through the method of proportional selection: calculate the cumulative selection probability q_i ($i = 1, 2, \dots, L$), and generate random number sequence r_j ($j = 1, 2, \dots, L$) in ascending order in the interval $(0, q_L)$. If $q_{i-1} < r_j < q_i$, the i -th individual is selected to enter the next generation.

- Step 4. Crossover

Crossover operation ensures that good traits can be inherited. In the real number coding mode, the operation is performed by arithmetic crossover. If two individuals, $a_i^k(t)$ and $a_j^k(t)$ ($k = 1, 2, \dots, n$), are selected randomly in the population for crossover, then the crossover calculation process is as follows:

$$\begin{cases} a_i^k(t+1) = a_i^k(t) \times (1 - b) + a_j^k(t) \times b \\ a_j^k(t+1) = a_j^k(t) \times (1 - b) + a_i^k(t) \times b \end{cases} \quad (C.3)$$

In the formula above, $a_i^k(t)$ and $a_j^k(t)$ are a pair of individuals before the crossover, $a_i^k(t+1)$ and $a_j^k(t+1)$ are the individuals after the crossover. This method is conducive to find the global optimal value.

- Step 5. Mutation

Mutation is an important way to ensure species diversity. This study implements non-uniform mutation operation. If the range of the gene value at the mutation point $a_i^j(g)$ is $[a_{\min}, a_{\max}]$, the new gene value $a_i^j(g+1)$ is determined by:

$$a_i^j(g+1) = \begin{cases} a_i^j(g) + (a_i^j(g) - a_{\max}) \times f(g), & r > 0.5 \\ a_i^j(g) + (a_{\min} - a_i^j(g)) \times f(g), & r \leq 0.5 \end{cases} \text{ where } f(g) = r_2 \times \left(1 - \frac{g}{G_{\max}}\right)^2 \quad (C.4)$$

where a_{\max} and a_{\min} are the upper and lower limits of allele, g represents current generation, G_{\max} is the maximum iterations, and r_1 and r_2 are random numbers in the range of $[0,1]$.

- Step 6. The load forecasting algorithm flow of the combinational model

GA realizes a stable and optimized selection process through inheritance and mutation, so that the population can evolve to a better search space area. The BP neural network optimized by genetic algorithm has good prediction accuracy and efficiency. The flow chart of GA-BP combined model is shown in Fig. C1.

C.2 BP neural network optimized by Particle Swarm Optimization algorithm (PSO)

The PSO algorithm is a global random search algorithm. The particles continue to iterate in the solution space before meeting the requirements. The PSO algorithm is a good approach for global optimum, but its search efficiency is low. On the contrary, the BP algorithm has a powerful ability to find local optimal solutions with little computation cost. By combining PSO and BP, the hybrid PSO-BP algorithm can find the global optimum faster. The basic idea of this hybrid algorithm is that at the beginning, the PSO algorithm is used to speed up the search. When the fitness function value is less than the preset value, the search mode changes to the gradient descent method. The process of PSO-BP algorithm can be summarized as follows:

- Step 1. Initialization of parameters

Parameter initialization includes population size, number of iterations, learning factors, and position and speed values within a limited range. In this step, a set of particles containing position and velocity information are randomly initialized. In an S -dimensional search space, a population of n particles is generated and denoted by $W = (W_1, W_2, \dots, W_n)$.

- Step 2. Determination of encoding mode

This step constructs the network topology structure according to the number of input and output parameters of the time series, and randomly generates a population particle to represent the initial value. The length of the code is $R \times S_1 + S_1 \times S_1 + S_1 + S_2$. Here R , S_1 and S_2 are the number of input layer nodes, the number of hidden layer nodes and the number of output layer nodes, respectively.

- Step 3. Fitness function

The definition of fitness function is similar to the GA-BP algorithm. This step assigns BP neural network weights and thresholds, input training samples for neural network training, and gets a network training output value when the set accuracy is reached. The fitness value is calculated corresponding to each particle position W_i .

- Step 4. Determination of extremum

In each iteration process, according to Eqs. (C.5)-(C.6), the speed and position of the particle itself are updated. A simple adaptive mutation operator is introduced to reinitialize the particle with a certain probability after the update of each particle. Then the fitness value of the new particle is calculated. The velocity of the i -th particle is denoted as $V_i = (V_{i1}, V_{i2}, \dots, V_{is})^T$, and its individual extremum is denoted as $P_i = (P_{i1}, P_{i2}, \dots, P_{is})^T$, the global extremum of the population is denoted as $P_g = (P_{g1}, P_{g2}, \dots, P_{gs})^T$. The particle updates its own speed and position through extreme values. The updated model is:

$$V_{id}^{k+1} = \omega V_{id}^k + c_1 r_1 (P_{id}^k - W_{id}^k) + c_2 r_2 (P_{gd}^k - W_{gd}^k) \quad (C.5)$$

$$W_{id}^{k+1} = W_{id}^k + V_{id}^{k+1} \quad (C.6)$$

where $d = 1, 2, \dots, S$, $i = 1, 2, \dots, n$, k is the current iteration number; V_{id} is the velocity of the particle; c_1 and c_2 are non-negative constants and called acceleration factors. r_1 and r_2 are random numbers distributed between [0,1].

- Step 5. The load forecasting algorithm flow of the combinational model

After meeting the requirements, the optimal particles obtained by the improved particle swarm algorithm are assigned to the BP neural network. Finally, the optimal value after BP neural network model training is obtained. The flow chart of the PSO-BP algorithm is summarized in Fig. C2.

References

- Abedrabbo, N., Pourboghrat, F., Carsley, J., 2007. Forming of AA5182-O and AA5754-O at elevated temperatures using coupled thermo-mechanical finite element models. *Int. J. Plast.* 23, 841–875.
- Ali, U., Muhammad, W., Brahme, A., Skiba, O., Inal, K., 2019. Application of artificial neural networks in micromechanics for polycrystalline metals. *Int. J. Plast.* 120, 205–219.
- Anna, Mogucheva, Diana, Yuzbekova, Rustam, Kaibyshev, Tatiana, Lebedkina, Mikhail, Lebyodkin, 2016. Effect of grain refinement on jerky flow in an Al-Mg-Sc alloy. *Metall. Mater. Trans. A*.
- Bonatti, C., Mohr, D., 2020. Neural network model predicting forming limits for Bi-linear strain paths. *Int. J. Plast.*, 102886.
- Buzolin, R.H., Lasnik, M., Krumpahls, A., Poletti, M.C., 2021. A dislocation-based model for the microstructure evolution and the flow stress of a Ti5553 alloy. *Int. J. Plast.* 136, 102862.
- Fu, Z., Mo, J., Chen, L., Chen, W., 2010. Using genetic algorithm-back propagation neural network prediction and finite-element model simulation to optimize the process of multiple-step incremental air-bending forming of sheet metal. *Mater. Des.* 31, 267–277.
- Gorji, M.B., Mozaffar, M., Heidenreich, J.N., Cao, J., Mohr, D., 2020. On the potential of recurrent neural networks for modeling path dependent plasticity. *J. Mech. Phys. Solids* 143, 103972.
- Huh, H., Ahn, K., Lim, J.H., Kim, H.W., Park, L.J., 2014. Evaluation of dynamic hardening models for BCC, FCC, and HCP metals at a wide range of strain rates. *J. Mater. Process. Technol.* 214, 1326–1340.
- Iftikhar, A., Li, Y.L., Kohar, C.P., Inal, K., Khan, A.S., 2021. Evolution of subsequent yield surfaces with plastic deformation along proportional and non-proportional loading paths on annealed AA6061 alloy: Experiments and crystal plasticity finite element modeling. *Int. J. Plast.*, 102956.
- Jang, D.P., Fazily, P., Yoon, J.W., 2020. Machine learning-based constitutive model for J2-plasticity. *Int. J. Plast.*, 102919.
- Jenab, A., Sari Sarraf, I., Green, D.E., Rahmaan, T., Worswick, M.J., 2016. The Use of genetic algorithm and neural network to predict rate-dependent tensile flow behaviour of AA5182-O sheets. *Mater. Des.* 94, 262–273.

- Johnson, G.R., Cook, W.H., 1983. A constitutive model and data for metals subjected to large strains, high strain rates and high temperatures. *Eng. Fract. Mech.* 21, 541–548.
- Jordan, B., Gorji, M.B., Mohr, D., 2020. Neural network model describing the temperature- and rate-dependent stress-strain response of polypropylene. *Int. J. Plast.* 135, 102811.
- Kabirian, F., Khan, A.S., Pandey, A., 2014. Negative to positive strain rate sensitivity in 5xxx series aluminum alloys: experiment and constitutive modeling. *Int. J. Plast.* 55, 232–246.
- Kessler, B.S., El-Gizawy, A.S., Smith, D.E., 2007. Incorporating neural network material models within finite element analysis for rheological behavior prediction. *J. Press. Vessel Technol.*
- Khan, A.S., Baig, M., 2011. Anisotropic responses, constitutive modeling and the effects of strain-rate and temperature on the formability of an aluminum alloy. *Int. J. Plast.* 27, 522–538.
- Kohar, C.P., Brahme, A., Imbert, J., Mishra, R.K., Inal, K., 2017. Effects of coupling anisotropic yield functions with the optimization process of extruded aluminum front rail geometries in crashworthiness. *Int. J. Solids Struct.* 128, 174–198.
- Li, X., Roth, C.C., Mohr, D., 2019. Machine-learning based temperature- and rate-dependent plasticity model: application to analysis of fracture experiments on DP steel. *Int. J. Plast.* 118, 320–344.
- Mayer, A.E., Krasnikov, V.S., Pogorelko, V.V., 2021. Dislocation nucleation in Al single crystal at shear parallel to (111) plane: molecular dynamics simulations and nucleation theory with artificial neural networks. *Int. J. Plast.*, 102953.
- Mozaffar, M., Bostanabad, R., Chen, W., Ehmann, K., Cao, J., Bessa, M.A., 2019. Deep learning predicts path-dependent plasticity. *Proc. Natl. Acad. Sci.* 116, 26414.
- Muhammad, W., Brahme, A.P., Ibragimova, O., Kang, J., Inal, K., 2021. A machine learning framework to predict local strain distribution and the evolution of plastic anisotropy & fracture in additively manufactured alloys. *Int. J. Plast.* 136, 102867.
- Palau, T., Kuhn, A., Nogales, S., Böhm, H.J., Rauh, A., 2012. A neural network based elasto-plasticity material model, ECCOMAS 2012 - European Congress on Computational Methods in Applied Sciences and Engineering. e-Book Full Papers 8861–8870.
- Pandya, K.S., Roth, C.C., Mohr, D., 2020. Strain rate and temperature dependent fracture of aluminum alloy 7075: experiments and neural network modeling. *Int. J. Plast.*, 102788.
- Settgast, C., Hüttler, G., Kuna, M., Abendroth, M., 2020. A hybrid approach to simulate the homogenized irreversible elastic-plastic deformations and damage of foams by neural networks. *Int. J. Plast.* 126, 102624.
- Sung, J.H., Kim, J.H., Wagoner, R.H., 2010. A plastic constitutive equation incorporating strain, strain-rate, and temperature. *Int. J. Plast.* 26, 1746–1771.
- Tsai, C.-Y., Lee, Y.-H., 2011. The parameters effect on performance in ANN for hand gesture recognition system. *Expert Syst. Appl.* 38, 7980–7983.
- Yamanaka, A., Kamijo, R., Koenuma, K., Watanabe, I., Kuwabara, T., 2020. Deep neural network approach to estimate biaxial stress-strain curves of sheet metals. *Mater. Des.* 195, 108970.
- Zerilli, F.J., Armstrong, R.W., 1987. Dislocation-mechanics-based constitutive relations for material dynamics calculations. *J. Appl. Phys.* 61, 1816.
- Zhang, A., Mohr, D., 2020. Using neural networks to represent von Mises plasticity with isotropic hardening. *Int. J. Plast.* 132, 102732.
- Zhu, L., Ruan, H., Sun, L., Guo, X., Lu, J., 2021. Constitutive modeling of size-dependent deformation behavior in nano-dual-phase glass-crystal alloys. *Int. J. Plast.* 137, 102918.